

Corotating Clumps Around Adolescent Low-Mass Stars: Four Years of TESS

—AUTHOR LIST & ORDER NOT FINAL,¹ LUKE G. BOUMA,^{1,*} RAHUL JAYARAMAN,² LYNNE A. HILLENBRAND,¹ GÁSPÁR Á. BAKOS,³ —SUGGESTED CONTRIBUTORS, PENDING DISCUSSION, COMMENTS, ANALYSES, ETC—², SAUL RAPPAPORT,² LUISA M. REBULL,¹ MAXIMILIAN N. GÜNTHER,⁴ GEORGE R. RICKER,² AND JOSHUA N. WINN³

¹Department of Astronomy, MC 249-17, California Institute of Technology, Pasadena, CA 91125, USA

²MIT Kavli Institute and Department of Physics, 77 Massachusetts Avenue, Cambridge, MA 02139

³Department of Astrophysical Sciences, Princeton University, 4 Ivy Lane, Princeton, NJ 08540, USA

⁴European Space Agency (ESA), European Space Research and Technology Centre (ESTEC), Keplerlaan 1, 2201 AZ Noordwijk, Netherlands

(Received —; Revised —; Accepted —)

ABSTRACT

Complex quasiperiodic variables (CQVs) are low-mass pre-main-sequence stars with nearly periodic optical modulation. The modulation is likely induced by dust or gas clumps in orbit at the Keplerian corotation radius. Here, we report new CQVs discovered in TESS short-cadence data collected between July 2018 and Sep 2022. Our search of 65,760 K- and M-dwarfs with $T < 16$ and $d < 150$ pc yielded 53 high-quality CQVs. Most of these discoveries are new, and they include the brightest ($T \approx 9.5$) and closest ($d \approx 20$ pc) examples of this class of object known, and probably also the most massive ($\approx 0.6\text{--}0.8 M_{\odot}$) and oldest (≈ 200 Myr). A few objects are outliers among outliers; LP 12-502 for instance shows a recurring “dip complex” with a period and total duration that are fixed over more than 1,000 cycles, but which in detail exhibits anywhere from four to eight local minima per cycle. LP 12-502 also displayed distinct superposed periods simultaneously, and showed drastic shape changes shortly after flares. Broadly speaking, we find that none of the CQVs maintain a fixed light curve shape over timescales of more than a few hundred cycles, and we revisit the arguments for why transient corotating material is the most viable explanation. In the future, we expect that our sample will facilitate modeling and observational efforts aimed at understanding these objects, and connecting them to the broader contexts of star, disk, and exoplanet evolution. For instance, if the transiting material is dust, then the rate of dip evolution implies that of order an asteroid belt’s worth of mass passes through these structures over their lifetime of $\approx 10^8$ years.

Keywords: Weak-line T Tauri stars (1795), Periodic variable stars (1213), Circumstellar matter (241), Star clusters (1567), Stellar magnetic fields (1610), Stellar rotation (1629)

1. INTRODUCTION

All pre-main-sequence stars vary in optical brightness, and the origin of such variability is, in most cases, understood. Well-explored sources of optical variability include inhomogeneities on stellar surfaces such as starspots and faculae (Basri 2021), occultations by gas-rich circumstellar disks (Bodman et al. 2017), and, in geometrically favorable circumstances, eclipses by stars and planets (Winn 2010). More exotic forms of optical variability relevant to this work include transiting exocomets (e.g. β Pic; Zieba et al. 2019) and disintegrating rocky bodies around both M-dwarfs (e.g. KOI-2700; Rappaport et al. 2014) and white dwarfs (e.g. WD 1145; Vanderburg et al. 2015).

Corresponding author: Luke G. Bouma
luke@astro.caltech.edu

* 51 Pegasi b Fellow

Data from K2 and TESS have yielded a new class of variable star whose root cause is only beginning to become clear: complex quasiperiodic variables (CQVs). These objects are identified phenomenologically using their optical light curves, which show nearly periodic troughs that can be either sharp or broad, often superposed on smooth spot-like modulation (Stauffer et al. 2017, 2018; Zhan et al. 2019). Some CQVs show up to eight local minima (dips) per cycle. Most are pre-main-sequence M-dwarfs without near-infrared excesses, ages of $\approx 5\text{--}150$ million years (Myr), and rotation periods of at most two days; they are observed to be $\approx 1\text{--}3\%$ of M-dwarfs younger than 100 Myr (Rebull et al. 2016; Günther et al. 2022). The dips can be chromatic, with a reddening law plausibly consistent with dust (Bouma et al. 2020; Günther et al. 2022; Koen 2023). And finally, while the dip shapes can “jump” between different depths and durations over less than one cycle, they more often evolve gradually, over tens to hundreds of cycles (e.g. Stauffer et al. 2017; Palumbo et al. 2022; Popinchalk et al. 2023).

A few competing explanations for what causes the complex quasiperiodic variability are shown in Figure 1. All young M-dwarfs are spotted, which produces flux variations over characteristic timescales of the rotation period, P_{rot} , and its half-harmonic, $0.5P_{\text{rot}}$. The observed dips occur over durations as short as $0.05P_{\text{rot}}$; a “starspot-only” scenario can be discarded for any object with sufficiently sharp dips (Stauffer et al. 2017; Koen 2021). The timescales and amplitudes of the flux variations instead require sharp geometries with material extrinsic to the stellar surface (e.g. Stauffer et al. 2017; Günther et al. 2022). The “clump” scenario invokes opaque dust clumps orbiting near the Keplerian corotation radius, which periodically eclipse the star (Stauffer et al. 2017; Sanderson et al. 2023). The “prominence” scenario invokes long-lived condensations of cool and dense marginally-ionized gas, embedded within the hotter corona, that would be centrifugally supported near corotation (Collier Cameron & Robinson 1989; Jardine & Collier Cameron 2019; Waugh & Jardine 2022). Such structures are analogous to quiescent prominences and filaments seen in the solar corona (see e.g. Vial & Engvold 2015), though at much larger relative distances from the stellar surface. A final possibility that has been suggested is one of a “screen”, in which the inner wall of a quiescent circumstellar disk blocks a portion of the stellar surface to produce sudden dips whenever spots come into view (Zhan et al. 2019).

The dust clump and prominence hypotheses seem most plausible. They are qualitatively similar, except that one invokes opacity from dust, while the other invokes opacity from gas, likely bound-free transitions in hydrogen or perhaps a molecular opacity. The screen scenario seems inconsistent with the degree of observed periodicity, the lack of infrared excess, and the observed lifetime of CQVs extending an order of magnitude longer than the $\approx 10^7$ year timescale typically quoted for primordial disk dispersal. However, unambiguous evidence in support of any one scenario has yet to be acquired. Such evidence might include a spectroscopic detection of silicate $10\mu\text{m}$ dust absorption during a dip, or perhaps detection of transient Balmer-line absorption as a function of cycle phase, similar to observations made in systems such as AB Dor (see the review by Collier Cameron 1999).

CQVs remain mysterious because they have been both hard to discover and hard to characterize. Discoverability is tied to rarity: CQVs comprise $\approx 1\%$ of the youngest $\approx 1\%$ of M-dwarfs (Rebull et al. 2018). Out of the millions of stars monitored by K2 and TESS, about 50 CQVs have been reported to date (Rebull et al. 2016; Stauffer et al. 2017, 2018; Zhan et al. 2019; Bouma et al. 2020; Günther et al. 2022; Popinchalk et al. 2023). The known CQVs are correspondingly faint; the initial K2 discoveries (Rebull et al. 2016; Stauffer et al. 2017) were M2-M6 dwarfs at distances $\gtrsim 100\text{ pc}$, yielding optical brightnesses of $V \approx 15.5$ to $V > 20$. This renders time-series spectroscopy at high resolution out of reach for current facilities, despite its potential utility in ruling between the models.

In this work, we aim to find bright and nearby CQVs, since these objects will be the most amenable to detailed photometric and spectroscopic analyses. To do this, we use 120-second cadence data acquired by TESS between July 2018 and Sep 2022 (Sectors 1-55; Cycles 1-4). We present our search methods in Section 2, and the properties of the resulting CQV catalog in Section 3. The evolution of many CQVs over a two-year baseline is described in Section 4, including a deep-dive into LP 12-502. We describe a few implications in Section 5, and conclude in Section 6.

A point on nomenclature. CQVs have been called “transient flux dips”, “persistent flux dips”, “scallop shells”, “batwings”, (Stauffer et al. 2017) “complex rotators”, (Zhan et al. 2019; Günther et al. 2022; Popinchalk et al. 2023) and “complex periodic variables” (Koen 2023). The CQVs should not be conflated with “dippers”, which are classical T Tauri stars with infrared excesses, and large-amplitude variability linked to obscuring inner disk structures and accretion hot spots (Cody et al. 2014; Robinson et al. 2021). With that said, a few similarities between CQVs and dippers do exist (see Sections 3.3 and 5.6). At the risk of introducing yet another standard, we hope to introduce a nomenclature that reflects how, when observed over timescales of more than tens of cycles, CQVs are almost but not exactly periodic. They are quasiperiodic. While the three-type classification scheme proposed by Stauffer et al. (2017) may indeed provide some helpful visual distinctions amongst the CQVs, it seems likely that they are all explained by a single underlying phenomenon, and so we opt to refer to them by a single empirically descriptive name.

2. METHODS

2.1. Stellar selection function

We analyzed the “short” 120-second cadence data acquired by TESS between July 2018 and Sep 2022 (Sectors 1-55). Specifically, we used the 120-second cadence light curve products produced by the Science Processing and Operations Center at NASA Ames (Jenkins et al. 2016). While the TESS data products also include full frame images with cadences of 200, 600, and 1800 seconds, we limited our scope in this work for the sake of simplicity in data handling. In exchange, we lose in both completeness and homogeneity of the selection function. While TESS cumulatively observed $\approx 90\%$ of the sky for at least one lunar month between July 2018 and Sep 2022, the 120-second cadence data were acquired for only a pre-selected set of stars over Sectors 1-26, and then a guest-investigator driven set of stars over Sectors 27-55 (Fausnaugh et al. 2021).

To assess the completeness of the resulting 120-second cadence data that is the basis of this study, we cross-matched TIC8 (Stassun et al. 2018) against the Gaia DR2 point-source catalog (Gaia Collaboration et al. 2018). We opted for Gaia DR2 rather than DR3 because the base catalog for TIC8 was Gaia DR2, which facilitated a one-to-one crossmatch using the Gaia source identifiers. This exercise showed that for $T < 16$ M-dwarfs, the TESS 2-minute data are roughly 50% complete at $\approx 50\text{ pc}$. At $< 20\text{ pc}$, $\gtrsim 80\%$ of the $T < 16$



Figure 1. Complex quasiperiodic variables (CQVs): *Top:* Phase-folded TESS light curves of three CQVs. Each is stacked over one month. Gray circles are raw 2-minute data; black circles bin to 300 points per cycle. Periods in hours are in the bottom right of each panel. Left-to-right, the objects are LP 12-502 (TIC 402980664; Sector 19), TIC 94088626 (Sector 10), and TIC 425933644 (Sector 28). *Bottom:* Cartoon models for the phenomenon. The dust clump scenario (lower left) and prominence scenario (lower center) both invoke centrifugally-supported material at the corotation radius. We disfavor the screen scenario (see Section 1).

M-dwarfs have at least one sector of short-cadence data; at >100 pc, $\lesssim 10\%$ of such M-dwarfs have at least one sector of short-cadence data. Armed with this understanding, we then used our cross-match between Gaia DR2 and TIC8 to select our stars of interest, which we defined as stars with 120-second cadence TESS light curves that satisfied

$$\begin{array}{lll} T < 16 & \text{(Bright for TESS)} & (1) \\ G_{\text{BP}} - G_{\text{RP}} > 1.5 & \text{(Red stars only)} & (2) \\ M_G > 4 & \text{(Dwarf stars only)} & (3) \\ d < 150 \text{ pc} & \text{(Close stars only)}, & (4) \end{array}$$

for $M_G = G + 5\log(\Omega_{\text{as}}) + 5$ the Gaia G -band absolute magnitude, Ω_{as} the parallax in units of arcseconds, and a geometric distance d defined by inverting the parallax and ignoring any zero-point correction. This selection function includes dwarf stars later than spectral types of $\approx K6V$ (Pecaut & Mamajek 2013) for which TESS can acquire 1% relative precision photometry in 1 hour of observation (Ricker et al. 2015). The target sample therefore includes 65,760 M-dwarfs and late-K dwarfs, down to $T < 16$ and out to $d < 150$ pc.

2.2. CQV discovery

Previous methods for finding CQVs have included visually examining stars known to be in young clusters (Rebull et al. 2016; Stauffer et al. 2017), and automatically flagging rapid rotators with a large number of strong Fourier harmonics (Zhan et al. 2019). The latter approach still requires visual vetting, since “stars with many Fourier harmonics” is a designation that includes objects such as eclipsing binaries or

multiple stars blended into a single photometric aperture. In this work, we implemented a new search approach based on counting the number of sharp local minima in phase-folded light curves, while also using the previously tested Fourier approach. We applied these two search techniques independently.

2.2.1. Counting dips

The dip counting technique aims to count sharp local minima in phase-folded light curves. CQVs will preferably have at least three such minima in order to be distinct from false positives such as synchronized and spotted binaries (“RS CVn” stars).

For our dip-counting pipeline, we began with the PDC_SAP flux for each sector, removed non-zero quality flags, and normalized the light curve to one by dividing out its median value. We then flattened the light curve using a 5-day sliding median filter, as implemented in `wotan` (Hippe et al. 2019). On the resulting cleaned and flattened light curve, we ran a periodogram search, opting for the Stellingwerf (1978) phase dispersion minimization (PDM) algorithm implemented in `astrobase` (Bhatti et al. 2021) due to its shape agnosticism. If a period below 2 days was identified, we reran the periodogram at a finer grid to improve the accuracy of the period determination.

Once a star’s period P was identified, we binned the phased light curve to 100 points per cycle. To separate “sharp” local minima from smooth spot-induced variability, we then iteratively fit penalized splines to the wrapped phase-folded light curve, excluding points more than two standard deviations away from the local continuum (Hippe et al. 2019).

The maximum number of equidistant spline knots per cycle is the parameter in this framework that controlled the meaning of “sharp”—we allowed at most 10 such knots per cycle, though for most stars fewer knots were preferred based on an ℓ^2 -norm penalty.

We then identified local minima in the resulting residual light curve using the SciPy `find_peaks` utility (Virtanen et al. 2020), which is based on comparing adjacent values in an array. For a peak to be flagged as significant, we required it to have a width of at least $0.02P$, and a height of at least twice the point-to-point RMS. This latter quantity is defined as the 68th percentile of the distribution of the residuals from the median value of $\delta f_i \equiv f_i - f_{i+1}$, where f is the flux and i is an index over time.

To correctly identify local minima near the edges of the phased light curve, which usually would cover phases $\phi \in [0, 1]$, we performed the entire procedure over a phase-folded light curve spanning $\phi \in [-1, 2]$, by duplicating and concatenating the ordinary phase-folded light curve. The free parameters we adopted throughout this analysis procedure, for instance the maximum number of spline knots per cycle, and how large and wide of a local minimum to consider a “true dip”, were chosen during testing based on their ability to correctly re-identify a large fraction (>90%) of known CQVs, while also being able to consistently reject common false positives such as rapidly rotating spot-induced variability and typical eclipsing binaries.

Overall, for a star to proceed to manual examination, we required that it have a peak PDM period below two days, and that it exhibited at least three sharp local minima (as algorithmically reported) in at least one observed TESS sector.

2.2.2. Fourier analysis

For the Fourier analysis, we followed Zhan et al. (2019).

TODO for Rahul or Saul: explain the approach, in a few paragraphs. Was the SAP_FLUX or PDCSAP used? etc.

2.2.3. Manual vetting

We visually assessed whether the objects found using the dip-counting (Section 2.2.1) and Fourier (Section 2.2.2) techniques were consistent with expectations for CQVs by assembling the data shown in Figure 2. We labeled a star as a “good” CQV if at least one TESS sector showed what we viewed as the unambiguous signatures of the class (short period; at least three dips or else otherwise oddly-shaped dips; relative stability over a timescale of 30 days). We independently noted stars that we thought could be CQVs, but that were more ambiguous.

Broadly speaking, the most common false positives for both the Fourier and dip-counting techniques were eclipsing binaries, spot-induced variability from rapid rotators, and variability from neighboring, off-target stars. Typical false positive rates from our dip-counting pipeline were 5:1, with 368 unique stars flagged, and about 20% being labeled either “good” or “possible” CQVs; for the Fourier pipeline,

the rate was X:Y, with ZZZZ unique stars flagged, and NN% being labeled “good” or “possible” CQVs.

2.3. Stellar properties

Ages—We estimated the stellar ages by making probabilistic spatial and kinematic associations between the CQVs and known clusters in the solar neighborhood. For most stars in our sample, we did this using BANYAN Σ (Gagné et al. 2018).¹ This algorithm calculates the probability that a given star belongs to one of 27 young clusters (or “associations”) within 150 pc of the Sun, by modeling the clusters as multivariate Gaussians in 3-D position and 3-D velocity space. We used the Gaia DR2 sky positions, proper motions, and distances to calculate the membership probabilities. BANYAN Σ in turn analytically marginalizes over the radial velocity dimension. The probabilities returned by this procedure are qualitatively useful, but should be assessed with caution due to the non-Gaussian nature of most groups within the solar neighborhood (see e.g. Kerr et al. 2021, Figure 10).

For a few cases where BANYAN Σ yielded ambiguous results, we consulted the meta-catalog of young, age-dated, and age-dateable stars within a kiloparsec from Bouma et al. (2022), and also searched the local volume around each star for co-moving companions.²

Effective temperatures, radii, and masses—We determined the stellar effective temperature and radii by fitting the broadband spectral energy distributions (SEDs); we then estimated the masses by interpolating against the sizes, temperatures, and ages against the PARSEC v1.2S models (Bressan et al. 2012; Chen et al. 2014).

For the SED fitting, we used `astroARIADNE` (Vines & Jenkins 2022). We adopted the BT-Settl stellar atmosphere models (Allard et al. 2012) assuming the Asplund et al. (2009) solar abundances, and the Barber et al. (2006) water line lists. The broadband magnitudes we considered included $GG_{\text{BP}}G_{\text{RP}}$ from Gaia DR2, $Vgri$ from APASS, JHK_s from 2MASS, SDSS r_{iz} , and the WISE 1-2 passbands. We specifically omitted UV flux measurements to avoid biasing our fit with any possible chromospheric UV excess. `astroARIADNE` compares the measured broadband flux measurements against pre-computed model grids, and by default fits for six parameters: $\{T_{\text{eff}}, R_{\star}, A_{\text{V}}, \log g, [\text{Fe}/\text{H}], d\}$. The distance prior is drawn from Bailer-Jones et al. (2021). The surface gravity and metallicity are generally unconstrained. And finally, given our particular use-case, we assumed the following priors for the temperature, stellar size, and extinction:

$$T_{\text{eff}}/\text{K} \sim \mathcal{N}(3000, 1000), \quad (5)$$

$$R_{\star}/R_{\odot} \sim \mathcal{T}_{\text{N}}(0.5, 0.3, 0.1, 1.5), \quad (6)$$

$$A_{\text{V}}/\text{mag} \sim \mathcal{U}(0, 0.2), \quad (7)$$

¹ https://github.com/jgagneastro/banyan_sigma, git commit 394b486

² <https://github.com/adamkraus/Comove>, git commit 278b372

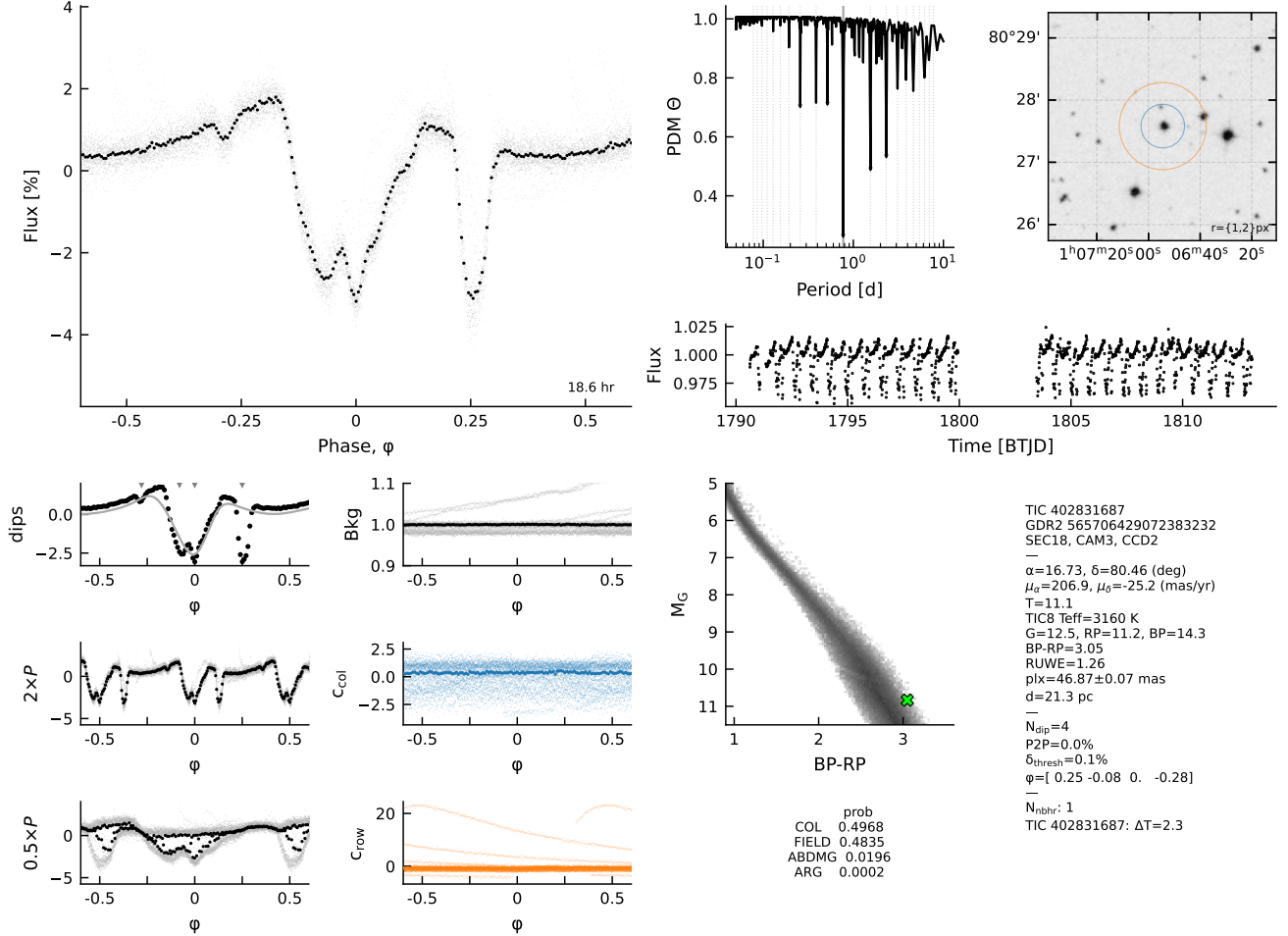


Figure 2. Validation plots used to label CQVs. The complete figure set, with one image per sector for each of 70 CQVs and CQV candidates is available online **For internal collaboration review:** <https://www.dropbox.com/scl/fo/zlj3txot4cvymfb22wewu/h?dl=0&rlkey=3ec5f9o5xewrixzfkhkdenopa>. Panels are as follows. *a*): Phase-folded light curve; gray points are raw 2-minute data and black points are binned to 200 points per cycle. *b*): Phase-dispersion minimization (PDM) periodogram. Dotted lines show up to the 10th harmonic and subharmonic. *c*): DSS finder chart, with 1- and 2-TESS pixel radius circles displayed for scale. *d*): Cleaned light curve, binned to 20-minute cadence, in Barycentric TESS Julian Date (BTJD). *e*): Phase-folded light curve, binned to 100 points per cycle. The gray line denotes the automated spline-fit to the wrapped phase-folded light curve, and small gray triangles denote automatically identified local minima. *f*): Phase-folded light curve at twice the peak period. *g*): Phase-folded light curve at half the peak period. *h*): Phase-folded time-series within the “background” aperture defined in the SPOC light curves. *i*): Phase-folded flux-weighted centroid in the column direction. *j*): Phase-folded flux-weighted centroid in the row direction. *k*): Gaia DR2 color-absolute magnitude diagram. The gray background denotes stars within 100 pc. *l*): Information from Gaia DR2, TIC8, and the automated dip-counting search pipeline. “Neighbors”, abbreviated “nbhr”, are listed within apparent distances of 2 TESS pixels if $\Delta T < 2.5$. *m*): BANYAN-Σ v1.2 association probabilities, calculated using positions, proper motions, and the parallax.

for \mathcal{N} the Gaussian and \mathcal{U} the uniform distributions, and $\mathcal{T}(\mu, \sigma, a, b)$ a truncated normal distribution with mean μ , standard deviation σ , and lower and upper bounds a and b . Using `Dynesty` (Speagle 2020), we statically sampled the posterior probability assuming the default Gaussian likelihood, and set a stopping threshold of $d\log \mathcal{Z} < 0.01$, where \mathcal{Z} denotes the evidence.

With the effective temperatures and stellar radii from the SED fit, we then estimated the stellar masses by interpolating against the PARSEC isochrones (v1.2S Chen et al. 2014). The need for models that incorporate some form of correction

for young, active M-dwarfs is well-documented (e.g. Stassun et al. 2012; David & Hillenbrand 2015; Feiden 2016; Somers et al. 2020). Plausible explanations for anomalous M-dwarf colors and sizes relative to model predictions include starspot coverage (e.g. Gully-Santiago et al. 2017), and potentially incomplete line lists (e.g. Rajpurohit et al. 2013). In the PARSEC models, Chen et al. (2014) performed an empirical correction to the temperature–opacity relation drawn from the BT-Settl model atmospheres, in order to match observed masses and radii of young eclipsing binaries. This is sufficient for our goal of estimating stellar masses. Given our

observed $\{\tilde{T}_{\text{eff}}, \tilde{M}_*, \tilde{t}\}$, and approximating their uncertainties as Gaussian $\sigma_{\tilde{T}_{\text{eff}}}$, $\sigma_{\tilde{M}_*}$ and $\sigma_{\tilde{t}}$, we evaluate a distance d between our observations and any model PARSEC grid-point $\{T_{\text{eff}}, M_*, t\}$ as

$$d^2 = \left(\frac{\tilde{T}_{\text{eff}} - T_{\text{eff}}}{\sigma_{\tilde{T}_{\text{eff}}}} \right)^2 + \left(\frac{\tilde{M}_* - M_*}{\sigma_{\tilde{M}_*}} \right)^2 + \left(\frac{\tilde{t} - t}{\sigma_{\tilde{t}}} \right)^2, \quad (8)$$

in order to assign equal importance to each dimension. The preferred model mass is then one that minimizes this distance, and is quoted in Table 1.

3. RESULTS

3.1. CQV catalog

Table 1 lists the 70 objects identified by our search. 53 objects demonstrated what we viewed as unambiguous characteristics of the CQV phenomenon in at least one TESS sector; we refer to these as the “high-quality sample”. The classification of the remaining 17 CQV candidates was ambiguous. Additional data from TESS or other instruments could help resolve their classification. The boolean quality column in the table divides the two classes. In the following, we will restrict our discussion to the high-quality sample.

The mosaic in Figure 3 shows phased light curves for the 53 CQVs. The objects are sorted first in order of the number of TESS 120-second cadence sectors in which they clearly demonstrated the CQV phenomenon, and secondarily by descending brightness. The top five objects by this metric are TIC 300651846 ($T=13.5$, 12 sectors); TIC 402980664 ($T=11.1$, 7 sectors); TIC 89463560 ($T=13.5$, 5 sectors); TIC 363963079 ($T=12.9$, 5 sectors); and TIC 294328887 ($T=14.2$, 4 sectors). The brightest five CQVs span $9.3 < T < 11.1$; the faintest five span $14.5 < T < 15.0$. The fastest five have periods spanning $3.6 \text{ hr} < P < 6.2 \text{ hr}$, and the slowest five span $27 \text{ hr} < P < 38 \text{ hr}$.

In terms of the light curve shapes, Figure 3 shows a broad range of variability, with anywhere from two to eight local minima per cycle. Some stars show relatively ordinary modulation during one portion of the phased light curve, and highly structured modulation in the remainder of the cycle (e.g. TIC 206544316, TIC 224283342, TIC 402980664). Others show structured modulation over the entire span of a cycle (e.g. TIC 2234692, TIC 401789285, TIC 425933644, TIC 142173958). Others show some mix between these two modes.

A small number of objects at first glance seem reminiscent of eclipsing binaries, such as TIC 193831684 or TIC 5714469. In these few cases, we believe that that are unlikely to be eclipsing binaries due to additional coherent variations in the light curves that are distinct from any binary phenomenology of which we are aware.

3.2. Ages

Of our 70 confirmed and candidate CQVs, 67 were associated with a nearby moving group or open cluster using BANYAN Σ . The relevant groups are listed in Table 1;

their ages span $\approx 5\text{-}200$ Myr. The most prodigious groups were Sco-Cen, Tuc-Hor, and Columba. Six CQVs were also identified in the Argus association (Zuckerman 2019), which serves as an indirect line of evidence supporting the reality, and youth, of that group. The yield in Sco-Cen is not particularly surprising, since Sco-Cen contains the majority of pre-main-sequence stars in the solar neighborhood. However, given the $\lesssim 10\%$ completeness of TESS beyond 100 pc, there are probably many more CQVs that remain to be discovered in Sco-Cen.

Of the three stars for which BANYAN Σ did not find any association, one (TIC 302160226) is a member of α Per ($t \approx 86 \pm 16$ Myr; Meingast et al. 2021; Boyle & Bouma 2023). For the other two (TIC 58084670 and TIC 141146667), we were not able to confidently associate either star with any young groups. However both do seem to clearly show the CQV signal over multiple TESS sectors, and both are photometrically elevated relative to the main sequence. For instance, both were noted by Kerr et al. (2021) as being in the “diffuse” population of < 50 Myr stars near the Sun.

Our search confirms that the CQV phenomenon persists for at least ≈ 150 Myr. Table 1 includes three ≈ 150 Myr CQVs in AB Dor (Bell et al. 2015), a ≈ 112 Myr old Pleiades CQV (Dahm 2015), and a similarly-aged Psc-Eri member (Ratzenböck et al. 2020). To our knowledge, TIC 332517282 in AB Dor was the previous record-holder for oldest-known CQV (Zhan et al. 2019; Günther et al. 2022); at least one unambiguous CQV (EPIC 211070495) and a few other candidates were also previously known in the Pleiades (Rebull et al. 2016).

The upper age limit for CQVs may even pass 200 Myr, based on the candidate membership of TIC 294328887 in the Carina Near moving group (Zuckerman et al. 2006). This group’s 200 ± 50 Myr age primarily rests on the lithium sequence of its G-dwarfs (Zuckerman et al. 2006), which shows a coeval population of stars older than the Pleiades and younger than the 400 Myr Ursa Major moving group. The formal BANYAN- Σ membership probability is however somewhat low, perhaps due to the missing radial velocity. This could be relatively easily resolved by acquiring even a medium-resolution spectrum. An independent assessment of the group’s kinematics using Gaia data, and its rotation sequence using TESS, could lend further credence in such an analysis.

3.3. Infrared excesses

As is typical for CQVs (Stauffer et al. 2017), most CQVs in our catalog did not show infrared excesses in the WISE1-4 bands. Visually inspecting the SEDs of our entire 70 star sample, we labeled two objects as having “good” infrared excesses (both W3 and W4), and three as “possible” infrared excess.

The two “good” IR excesses belonged to “ambiguous” CQVs TIC 193136669 (TWA 34) and TIC 57830249 (TWA 33). Both are in the TW Hydræ association (≈ 10 Myr), and have relatively long periods of 38 hr and 44 hr respectively. In our initial labeling, we labeled both

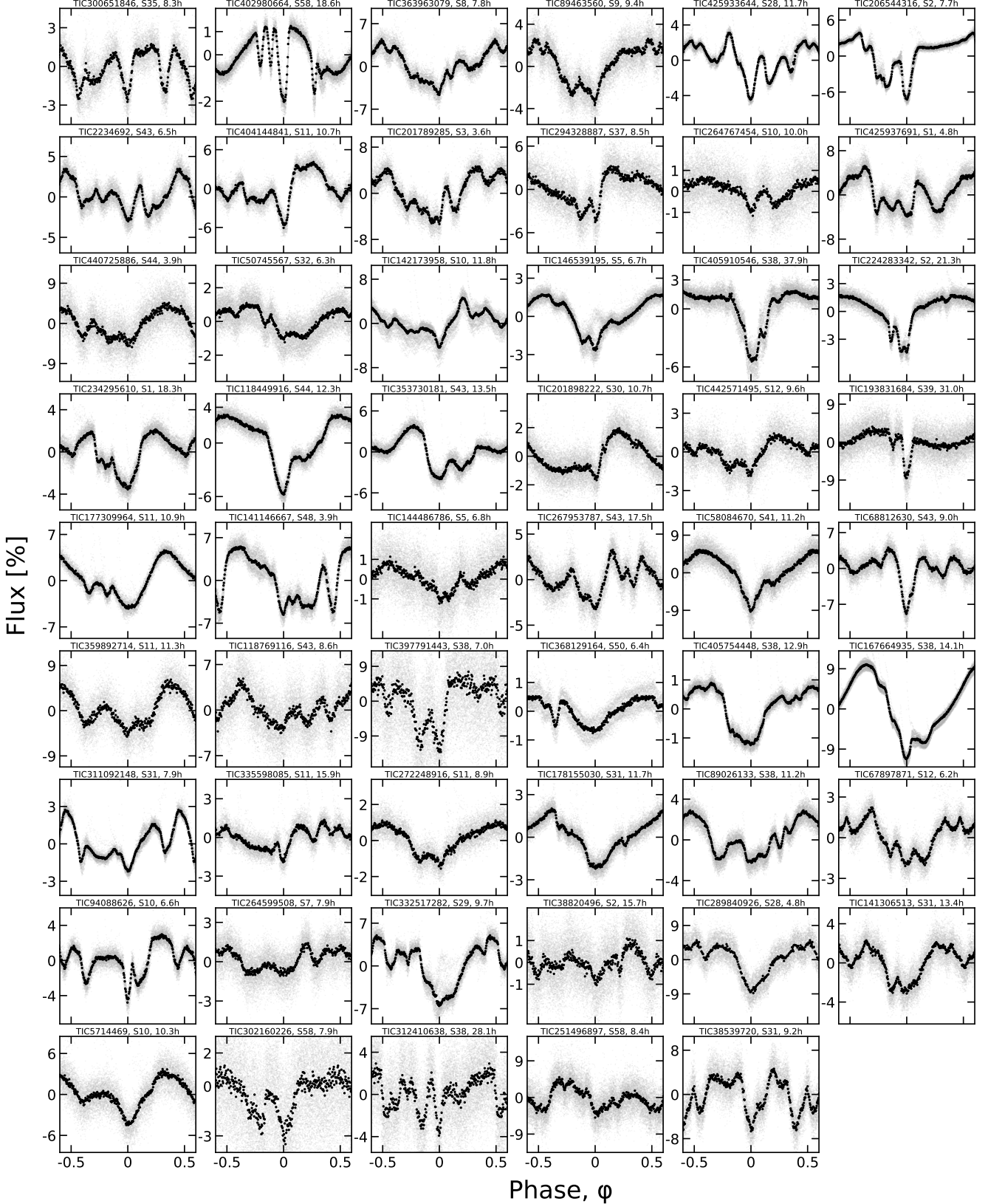


Figure 3. CQVs found in the TESS 2-minute data. Phased TESS light curves over one month are shown for 53 CQVs. Gray are raw 2-minute data; black bins to 300 points per cycle. Each panel is labeled by the TIC identifier, the TESS sector number, and the period in hours. Objects are ordered such that sources with the most TESS data available are on top (see Section 3.1).

as “ambiguous” CQVs because the dips in their light curves did not show the rigid periodicity typical of CQVs; their periods were also relatively long. After labeling them, inspection of further sectors clarified that both sources are dippers (see plots in Figure 2). Independently, TIC 193136669 has a cold molecular disk based on observed 1.3 mm continuum emission and resolved Keplerian $^{12}\text{CO}(2-1)$ emission (Rodriguez et al. 2015). It was also labeled a dipper by Capistrant et al. (2022); we agree with their designation, but nonetheless leave it in our catalog as an indication of possible ambiguities in our search process. TIC 57830249 (TWA 33) also has previously detected 1.3 mm continuum emission (Rodriguez et al. 2015), suggestive of cold dust grains being present. It is also a dipper. Section 5.6 highlights plausible evolutionary connections between CQVs and dippers in light of these “misclassifications”.

Our three “possible” infrared excesses were TIC 405910546, 289840926, and 244161191. After a literature search, we concluded that none have clear evidence for the presence of a disk. TIC 405910546, in LCC, shows a unique TESS light curve, reminiscent of a $P=38$ hr singly-eclipsing binary, except with additional substructure during each eclipse that resembles the CQV phenomenon more than any other variability of which we are aware. TIC 289840926 (β Pic moving group, $P=4.8$ hr), shows what we believe is a clear CQV signal, but has no definitive evidence for a large, dusty disk. TIC 244161191 (TOI-278), in Columba, also has no definitive evidence for a large disk. It is however “multi-periodic”—in addition to the 7.17 hr CQV signal, this source shows a superposed 8.39 hr sinusoidal signal, probably from an unresolved neighboring star.

4. CQV EVOLUTION

4.1. Evolution over two year baseline

Figure 4 shows “before” and “after” views of 27 CQVs for which TESS 120-second cadence observations were available at least two years apart. Such a baseline was available for 32 of the confirmed 53 CQVs in our catalog; for plotting purposes we show the brightest 27. We have phased each sector to its own local minimum because for most of the sources we do not know the period at the precision necessary to be able to accurately propagate an ephemeris over two years.

Of these 27 CQVs in Figure 4, a few show clear signs of the CQV phenomenon in one sector, and marginal or non-existent signs in the other. While there is subjectivity in this assessment, to our eyes cases for which at least one sector would be flagged as “ambiguous” include TIC 368129164 (Sector 23 might be labeled an EB), TIC 177309964 (Sector 38 would be simply a rotating star), TIC 404144841 (Sector 38 looks like a rotating star), TIC 201898222 (Sector 3 looks like a rotating star), TIC 144486786 (Sector 32 might be an RS CVn), and TIC 38820496 (Sector 28 might be an RS CVn). TIC 193831684, assessed on a single-sector basis, would probably be labeled an eclipsing binary—in fact, Justesen & Albrecht (2021) implicitly have already given this source such a label. However, based on the shape evolution between Sectors 13 and 39, it is a CQV. Based

on the fraction of sources overall that “turned off”, the observed shape evolution implies that CQVs have a duty cycle of $\approx 75\%$. This type of correction is likely worth including in population-level estimates of how intrinsically common CQVs are in the low-mass stellar population (e.g. Günther et al. 2022).

4.2. Evolution over adjacent sectors, & LP 12-502

4.2.1. LP 12-502 observations

While many CQVs had multiple sectors of adjacent or nearly-adjacent data, LP 12-502 (TIC 402980664; $d=21$ pc, $J=9.4$, $T=11.1$) stood out due to the quality and content of its data. Figure 5 shows all available data from Sectors 18, 19, 25, 26, 53, 58, and 59, split into successive orbits; the star was observed at 120-second cadence whenever it was observable by TESS. We binned the light curve to 15-minute intervals for visual clarity, and required at least one (120-second cadence) flux measurement per bin. Points more than 2.5σ above the median are drawn in gray, also for visual clarity. Missing data are not drawn. Figure 6 then shows the same data, but stacked into successive TESS orbits spanning half a lunar month each.

The average period, determined by measuring the PDM peak period over each sector independently, was $\langle P \rangle = 18.5560$ hr. The range between the maximum and minimum sector-specific periods was measured to be about one minute. Based on this range, the star’s period is stable to at least one minute (± 0.017 hr) over the three year baseline. However, in detail, a period shift of ± 1 minute would yield major phase drifts over the baseline; that time interval corresponds to roughly $1/1000^{\text{th}}$ of a period, and we have observed 1500 cycles. The achievable period precision, σ_P , can be estimated as

$$\sigma_P = \frac{\sigma_\phi P}{N_{\text{baseline}}}, \quad (9)$$

for N_{baseline} the number of cycles in the observed baseline and σ_ϕ the phase precision with which any one feature (e.g. a dip, or the overall shape of the sinusoidal envelope) can be tracked. Assuming $\sigma_\phi \approx 0.01$ yields an expected period precision $\sigma_P \approx 0.45$ sec $\approx 1.2 \times 10^{-4}$ hr. By visually fine-tuning over a grid in period, we eventually found $P = 18.5611 \pm 0.0001$ hr, which seems to track certain features in the LP 12-502 light curve over its entire baseline.

What exactly is observed? For the first 64 cycles, the star shows a pattern reminiscent of an eclipsing binary, with four obvious local minima. We dub these dips $\{1, 2, 3, 4\}$ at phases $\{-0.28, -0.08, 0, 0.25\}$, respectively. Over cycles 0 to 64, the depth of dips 1 and 3 remain roughly fixed. However dip 4 decreases in depth by about 2%, while dip 2 increases in depth, by about the same amount (see Figure 6). During cycles 48-64, a fifth dip may also be emerging, in the main “large” dip group.

There is then a 6-month (184 cycle) gap to Cycles 248-315, which show two intricately structured dip complexes, plus a small leading dip. The single leading dip is present at the same phase as in cycles 0-64, and is therefore likely to be the

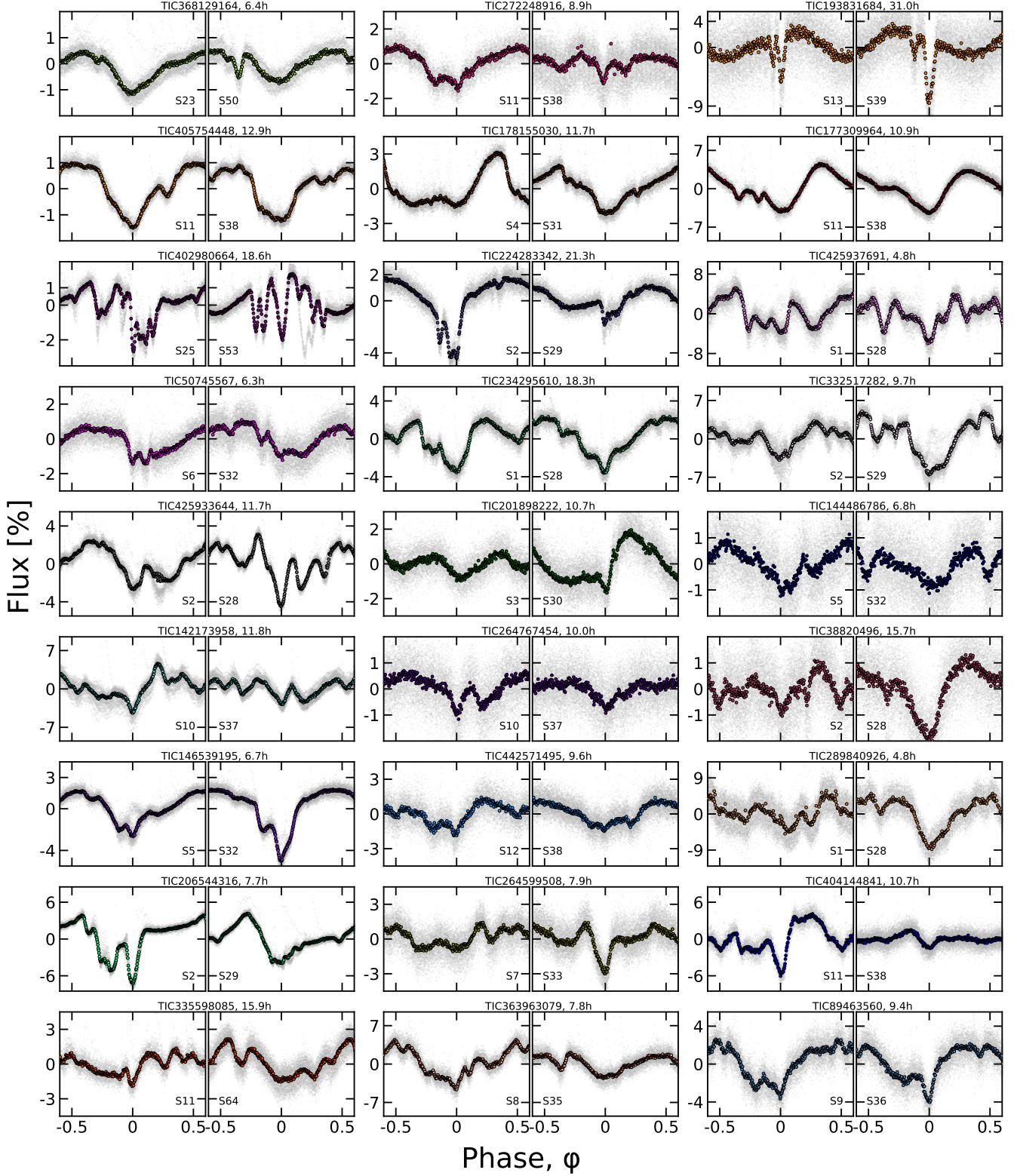


Figure 4. CQVs keep their periods but change their shapes. 32 of our 53 CQVs from Figure 3 had 120-second cadence TESS data available for a baseline of at least two years; the 27 brightest are shown here. Each panel shows one sector of TESS data, and is phased to its deepest minimum in flux. Each panel's title shows the TIC identifier and approximate period in hours. Text insets show the TESS sector numbers, which generally span two years, or at least 1,000 cycles. The vertical scale is fixed across sectors to clarify shape changes. Gray circles are raw 2-minute data; colored circles bin to 300 points per cycle.

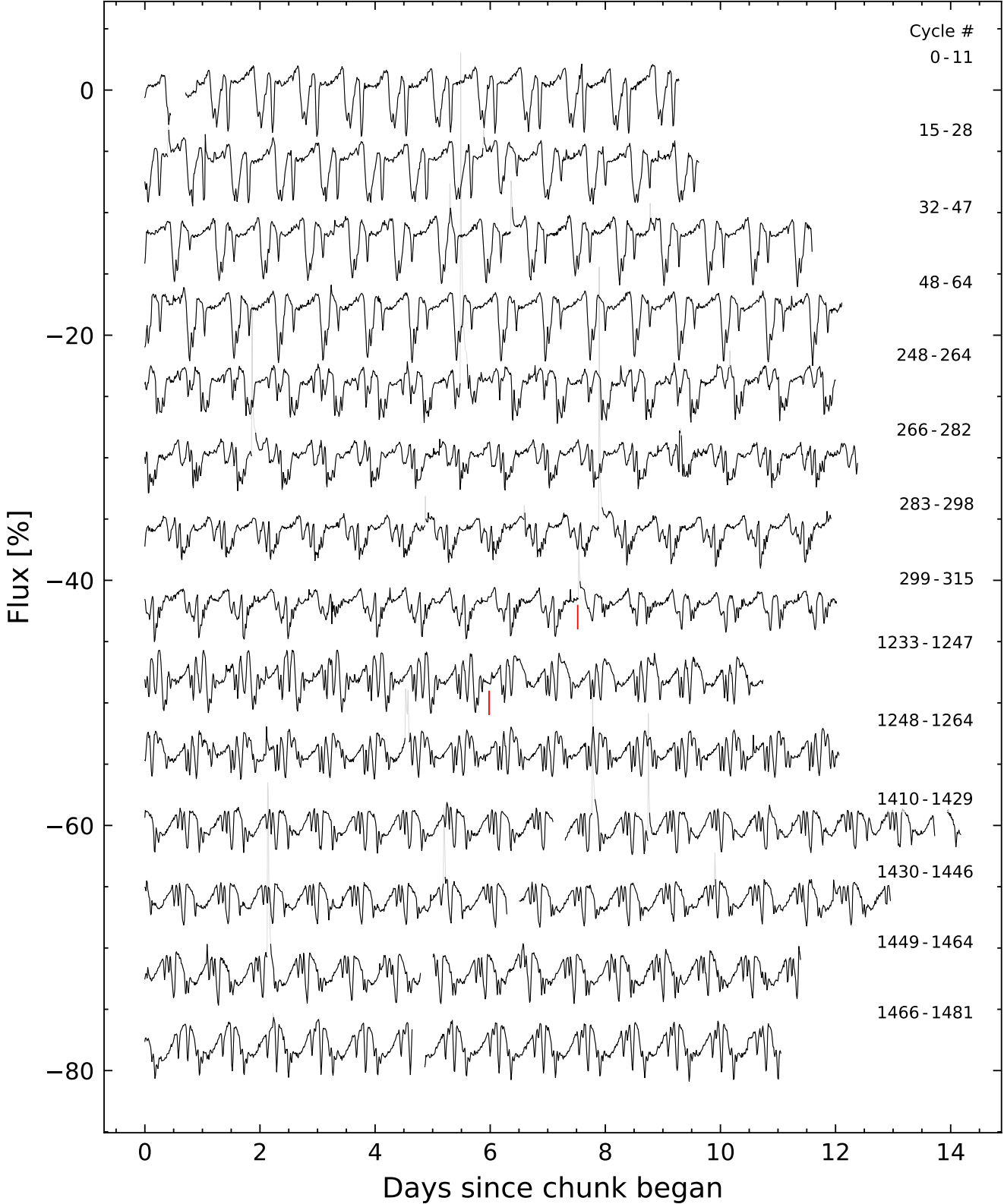


Figure 5. LP 12-502 (TIC 402980664) light curve, where each time chunk represents one TESS orbit. Data were acquired in Sectors 18-19, 25-26, 53, and 57-58. Flares are drawn in gray. The red vertical lines highlight apparently instantaneous state changes in the shape of the dip pattern. The light curve is binned to 15-minute intervals so that there are 96 points per day, and each point is connected by a line. Data gaps longer than 15-minutes are not interpolated; if data are missing, nothing is plotted.

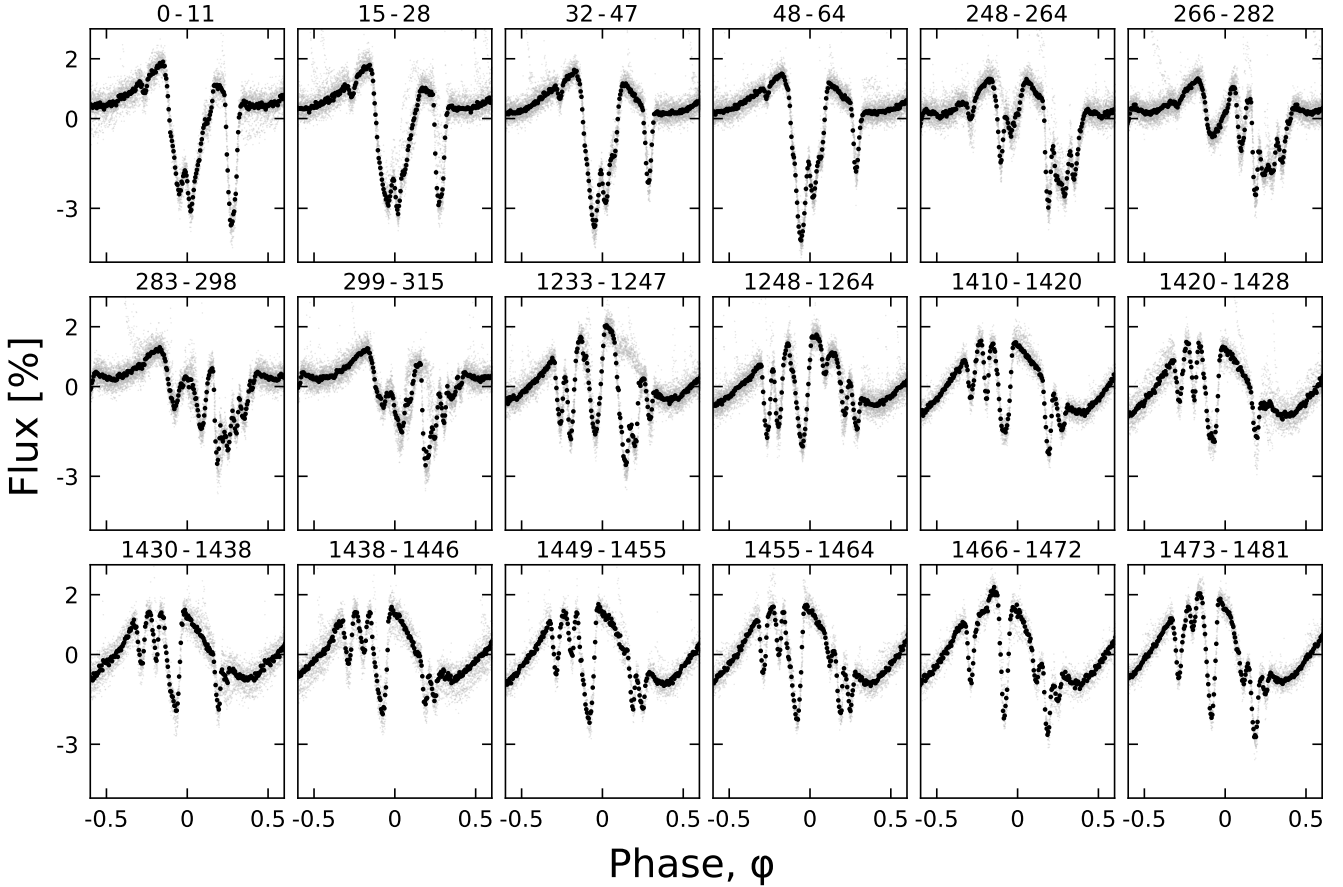


Figure 6. Evolution of LP 12-502 ($P=18.6$ h) at fixed period and epoch over three years. Each panel shows one (stacked) TESS orbit; small text denotes relative cycle number. There are 200 binned black points per cycle. The TESS pointing law dictates time gaps; larger gaps tend to yield larger shape changes. The dips usually evolve over tens to hundreds of cycles. However cycles 1233-1264 show a dip that “switched” from a depth and duration of 3% and 3 hr to 0.3% and 1 hr over less than one cycle (cf. Figure 5).

same structure. Along a similar line of logic, it seems plausible that the first “dip complex” during cycles 248-264 represents an evolution of the initial complex seen during cycles 0-64, though with greatly reduced depth. During cycles 266-310, an additional local minimum develops between the two complexes; this feature is best visualized on the river plots (Appendix A), and we discuss its (shorter) period below.

The second dip complex during cycles 248-315 shows the most substructure. During e.g. cycles 283-298, this single complex shows six local minima. The deepest dip is sharp: it shows a flux excursion of 3.5% over about 22 minutes ($0.02 P$), which is the steepest slope exhibited anywhere in the LP 12-502 remarkable dataset. After the sharp dip, there is a roughly exponential fall-off spanning about a quarter of a period, punctuated by coherent local minima and maxima which in detail (Appendix A) have slightly longer periods than the sharp dip. The sharp leading dip only decreases in depth following a sudden state-switch at BTJD 2030.7 (cycles 299-315), which happens during a flare (Figure 5). The trailing dips remain thereafter.

Sectors 53–58 (cycles 1233-1481) are comparatively tame; they showed only four to six dips per cycle. Some dips remain stable in depth and duration over this five month interval. Other dips grow, like the one at $\phi = +0.06$ between cycles 1499 and 1481. Other dips, such as the one at $\phi = +0.12$ in cycles 1233-1264, disappear entirely. The most dramatic state switch occurs during cycles 1233-1247, when a large dip “switches” from a depth of 3% and duration of 3 hours to a depth of 0.3%, and a duration of 1 hour.

4.2.2. Lessons from LP 12-502

STATE-SWITCHES REVEAL DIP INDEPENDENCE—The state-switches seen in cycles 1233-1247 and 299-315 confirm that dips can disappear in less than one cycle, a point which has been previously appreciated (Stauffer et al. 2017). What is new in these particular changes is that the morphology changes show that the dips can be *independent* and *additive*. For example, throughout cycles 1233-1264, there are three local minima between phases of 0 and 0.3. They all have identical ingress times. The shape change during the transition implies that the leading dip that “turned off” (re-

duced its depth and duration), while the trailing two dips remained fixed. In other words, the structures producing these dips are independent to the degree that one can undergo a severe change while the others remain essentially identical. The state switches during cycles 248-264 and 299-315 share the same characteristic: it is always the *leading* dip of a complex that “switches off”, leaving the (fixed-depth) trailing dips in its wake.

SLOW GROWTH; RAPID DEATH—Although there are a few instances in which we observe dips switch off over less than one cycle, dip growth seems to happen more slowly. For instance, the dip that grows between phase 0 and 0.1 between cycles 260-290 begins to become visible around BTJD 1993.2, and grows in depth by about 2% over about six cycles, to become easily detectable by eye by BTJD 1997.7. The evolution of this particular dip is most clear in the river plots. The evolution of the latter dip group in cycles 1410-1481 is another example of this slow mode of dip growth.

DIP DURATIONS—The shortest dip duration for any of the individual LP 12-502 dips seems to be $\approx 0.06 P \approx 1.08$ hr. In comparison, using the stellar radius and mass derived in Section 2.3, the characteristic timescale $T_{\text{dur}} \equiv R_* P / (\pi a)$ for the transit of a point-source at corotation is 1.03 hr (**uncertainties?**). This means that while some of the LP 12-502 dips are sufficiently long to require structures that are extended in orbital azimuth, the durations of other dips are consistent with effective radii for the occulting material $R_{\text{eff}} \ll R_*$. This implies $a/R_* \approx 5.8$ for this material, and so the analogous timescale at the stellar surface is about six times slower.

DIP PERIODS—Most of the LP 12-502 dips recur with a period of $P = 18.5611 \pm 0.0001$ hr. However the river plots (Appendix A) reveal multiple distinct periodicities in the light curve for specific dips. For instance, in sectors 25-26, the local minimum that develops around cycle 262 has a period faster than the mean period by $\approx 0.1\%$, while some of the trailing local minima in the main dip complex have periods slower than the mean period, by $\approx 0.04\%$. In addition to the fundamental period, we were able to identify at least four distinct periods shown by specific dips over the full Sectors 18-59 dataset, including periods at 18.5683, 18.5672, 18.5473, and 18.5145 hr, with a typical measurement uncertainty of ≈ 0.0002 hr. If each period corresponds to a dust clump, then this implies that multiple distinct clumps can orbit the star simultaneously, at marginally different separations.

5. DISCUSSION

5.1. Typical and extreme CQVs

Figure 7 shows some of the derived properties for our CQV catalog, and contrasts them against both the target star sample (top panels), and the population of rotating stars in the Pleiades from Rebull et al. (2016). Generally, CQVs are much younger than typical field stars. In terms of their rotation, relative to the Pleiades, they are among the more rapidly rotating half of M-dwarfs. The dearth of $T > 15.5$ CQVs in our sample, despite our search extending to $T=16$, is a consequence of the 120-second selection function, not detection sensitivity.

The closest CQV in our catalog is DG CVn (TIC 368129164; $d=18$ pc), a member of AB Dor. To our knowledge, this manuscript is the first time that it has been noted as a CQV. The three brightest CQVs are DG CVn ($T=9.3$), TIC 405754448 ($T=9.6$), and TIC 167664935 ($T=10.3$). The shortest period belongs to TIC 201789285, at 3.64 hr. The longest period belongs to TIC 405910546, at 37.9 hr. If the latter source turns out to be an eclipsing binary, the next-longest would be TIC 193831684 (31.0 hr).

The lowest mass ($\approx 0.12 M_\odot$) belongs to TIC 267953787. The catalog contains a few other stars with similar mass. Given the small number of sub-stellar mass objects in our target sample, this suggests that future studies of brown dwarf photometric variability might also yield complex quasiperiodic variables, though there could be degeneracies in interpretation with planetary surface features such as clouds and latitudinal bands (e.g. Apai et al. 2021; Vos et al. 2022).

The most massive CQV in our sample is a subject of some interest. To date, the only stars reported to show the CQV phenomenon are M-dwarfs, with typical stellar masses $\lesssim 0.3 M_\odot$ (Günther et al. 2022). TIC 405754448 and 405910546 however appear to have masses of 0.82 and $0.60 M_\odot$ respectively. The next-highest masses are $\approx 0.40 M_\odot$. The masses for the former two objects are consistent with their CAMD locations, and their membership in LCC. Based on its light curve morphology, TIC 405910546 should be studied in greater depth, to confirm it is not an eclipsing binary. TIC 405754448 similarly shows distinct morphology from many of the CQVs in Figure 3, in that it has some of the lowest amplitude dips. Nonetheless, both of these objects seem to suggest that the CQV phenomenon extends up in mass to pre-main-sequence K-dwarfs.

5.2. CQVs are quasiperiodic

A periodic signal repeats exactly; the CQVs do not (Figure 4). While their periods appear to remain constant to within measurement precision over thousands of cycles, the light curve shapes evolve over 10 to 1,000 cycles. They are therefore *quasiperiodic*. This observation is consistent studies by Günther et al. (2022) and Popinchalk et al. (2023). However it marks a qualitative departure from the “persistent” vs. “transient” flux dip distinction described by Stauffer et al. (2017); since all CQV dips seem to be transient over timescales of more than 1,000 cycles (Figure 4).

With that said, one might expect a truly quasiperiodic process to be able to explore all phase angles with equal weight. LP 12-502, and perhaps other CQVs, seem to have preferred phases. For LP 12-502, all of the dips happen over phases corresponding to only two thirds of the period (Figure 6). The remaining third seems to be “out of limits” for any dipping material. This could be evidence that some aspect the stellar magnetic field is strongly asymmetric, and can generate and hold extrinsic material at corotation, but only over two thirds of the equatorial circle. Alternatively, the source of the material (e.g. a planetesimal swarm) might be distributed over an arc of the same angular extent (240°). We favor the former explanation, for reasons discussed below.

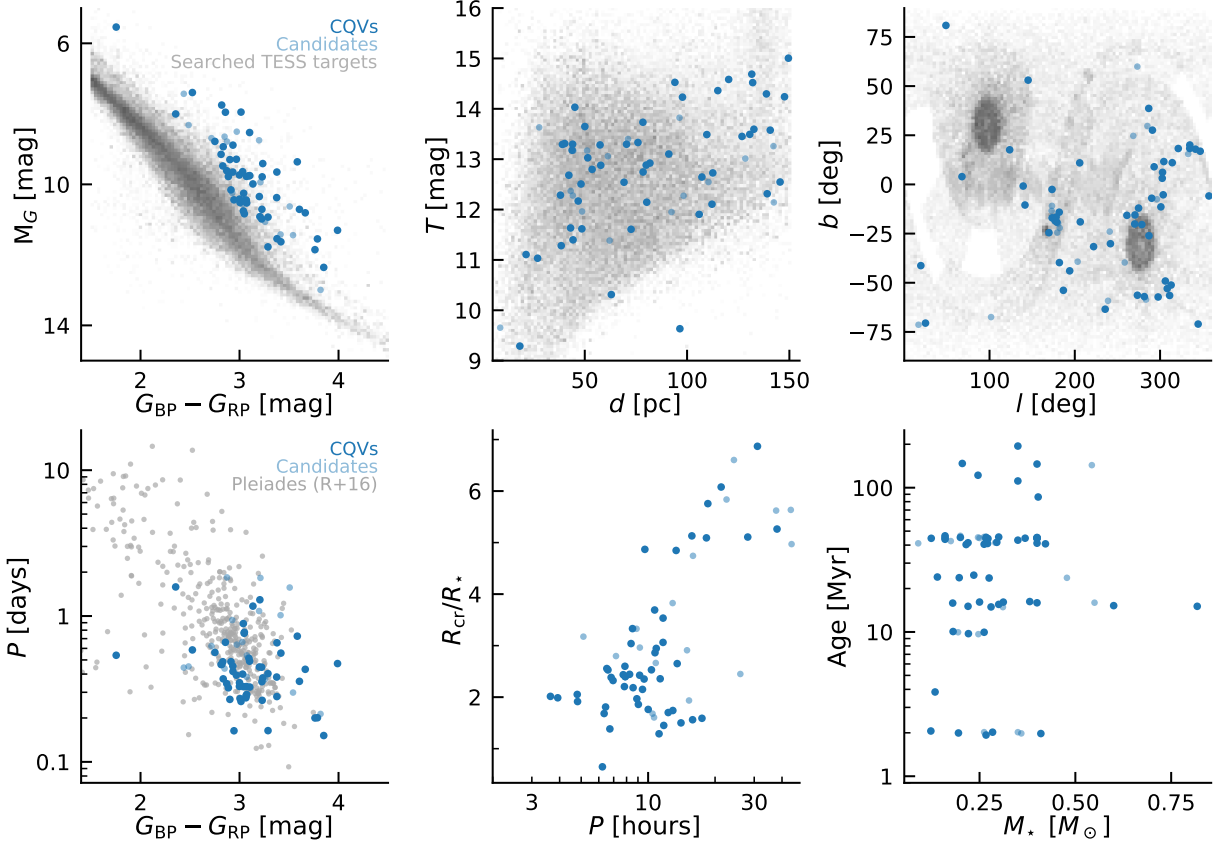


Figure 7. Properties of CQVs identified by our search. The 53 bona fide CQVs in Table 1 are the dark blue circles; 17 ambiguous CQV candidates are light blue circles. The top panels show the 65,760 target stars with 120-second cadence TESS data as the shaded gray background; darker regions correspond to a larger relative number of searched stars. The lower-left panel compares the rotation–color distribution of CQVs against the rotation periods of K- and M-dwarfs in the Pleiades from [Rebull et al. \(2016\)](#). The lower-middle panel plots the derived corotation radii $R_{\text{cr}} = (GM/\Omega^2)^{1/3}$ in units of stellar radii against the measured CQV periods, in units of hours.

5.3. Dip asymmetries and dust geometries

The asymmetry of a dip can help diagnose the optical depth of the occulting material as a function of orbital phase angle. Sharp leading edges with trailing exponential egresses for instance have been previously seen for transiting exocomets and disintegrating rocky bodies (e.g. [Rappaport et al. 2012](#); [Brogi et al. 2012](#); [Vanderburg et al. 2015](#); [Zieba et al. 2019](#)).

Examining Figure 3, it is not obvious whether CQVs as a whole show any preference for sharper ingresses, or sharper egresses. In some cases (e.g. TIC 425933644), the continuum itself is not well-defined, and so the meaning of “ingress” and “egress” are not clear. In others, such as Sector 36 of TIC 89463560, there is a single clear sharp ingress with an exponential egress, which could be directly fit using e.g. a model analogous to those used for exocomets (e.g. [Zieba et al. 2019](#)). The main quantities of interest in such models would be the exponential decay time- and therefore length-scale, as well as the impact parameter and the inferred transit depth (and its implications for the equivalent “radius” of the transiting cloud). Although we briefly explored such models, it quickly became clear that careful mod-

eling of sources such as LP 12-502 merits its own in-depth study. Connections could likely also be made to the toroidal geometries that can be produced by outflowing atmospheres of transiting planets (e.g. [McCann et al. 2019](#); [MacLeod & Oklopčić 2022](#)).

5.4. Dust, or gas?

We believe that the most likely scenarios to explain CQVs are either the dust clump scenario or the prominence scenario (Figure 1). Both invoke clumpy material that would be centrifugally supported at the corotation radius. The prominence idea has a longer history, based on analogy with quiescent prominences/filaments observed to exist in the solar corona for up to a few weeks (see [Vial & Engvold 2015](#)). In an extrasolar context, spectroscopic detections of transient Balmer- and resonance-line absorption seen for stars such as AB Dor and Speedy Mic (e.g. [Collier Cameron & Robinson 1989](#); [Jeffries 1993](#); [Dunstone et al. 2006](#); [Leitzinger et al. 2016](#)) led to the interpretation that the data could best be explained by similar structures: cold, minimally ionized hydrogen clouds or filaments that scatter chromospheric emission from the star to produce the observed spectroscopic line vari-

ations (see Collier Cameron & Robinson 1989). The short-term mechanical stability of such gas configurations is theoretically plausible (Ferreira 2000; Waugh & Jardine 2022), and the interpretation of this class of observations seems at least somewhat secure.

Any link between the dense gas clumps (prominences) that likely exist around rapidly rotating low-mass stars and the CQV phenomenon has yet to be made. A simple visual examination of the TESS light curves for five prominence-hosting systems studied by Jardine & Collier Cameron (2019)—AB Dor, Speedy Mic, LQ Lup, HK Aqr, and V374 Peg—revealed no obvious CQV behavior, though all show differential evolution, and Speedy Mic shows two closely-spaced periods and a strong beat. Spectroscopically observable prominences do not imply CQV-like dips.

The difference between the prominence and dust clump scenarios is essentially only in whether the occulting material of interest is neutral hydrogen, or dust. In the phrasing of the “frozen flux” condition of ideal rigid field magnetohydrodynamics, the tendency of both to become trapped at the corotation radius in the equatorial plane is tied to how of the four relevant forces (gravity, Lorentz, inertial Coriolis, and inertial centrifugal), the Lorentz and Coriolis only act perpendicular to field lines, while gravity and the centrifugal force are in balance at R_{cr} (see Townsend & Owocki 2005, Sec. 2). The magnetic field strength is only relevant in this formulation of the system in that we must have $R_{\text{sonic}} < R_{\text{cr}} < R_{\text{Alfvén}}$ in order for closed loops to exist that can support prominences (Jardine & Collier Cameron 2019) **lgb todo: verify & dejargonify!**. In detail however, whether such magnetic fixed points lie in the equatorial plane, or elsewhere, depends on the star’s magnetic field geometry (Sanderson et al. 2023).

5.4.1. Can gas absorption reproduce the observed chromaticity?

The strongest argument for why neutral hydrogen is an unlikely occulting source is that CQVs show broadband flux variations that are deeper in the blue than in the red.

Based on our reading of Gray (1992, Ch. 8), it seems challenging to get neutral hydrogen to have this type of chromaticity. Bound-bound absorption provides opacity only at narrow resonant lines. Bound-free absorption can provide wavelength-dependent opacity, but the absorption coefficients generally grow with increasing wavelength, rather than shrink as one needs in order to get deeper absorption in the blue than in the red. H^- fails as a viable opacity source for the same reason: its absorption coefficient peaks near 8500 Å, and is an order of magnitude smaller at $\approx 3000 \text{ Å}$. (Gray 1992, following Wishart 1979). Thompson scattering is also ruled out, because it is gray. Dust, with its larger absorption cross-section in the blue than the red (Cardelli et al. 1989), is to our knowledge the most obvious opacity source.

While the reasoning above seems fairly convincing, it has a flaw. The argument presented above would imply that regardless of a star’s temperature, if relative depths of a dip are seen to be deeper in the blue than in the red, then it is hard to get hydrogen to do it. There is however a rapidly rotating magnetic B-star, σ Ori E, which shows dips that are deeper in

the blue than in the red (Hesser et al. 1977). Photometric and spectroscopic observations of this star have been understood in terms of absorbing circumstellar material, analogous to the geometries we are discussing for much cooler M-dwarfs (Townsend et al. 2005). This material however is unlikely to be dust, due to the relevant sublimation timescales. The opacity is instead thought to be sourced from bound-free absorption from neutral hydrogen (Townsend et al. 2005). Separate and smaller amplitude emission in that system may also come from electrons scattering photospheric light toward the observer when the clouds are not in transit (Berry et al. 2022).

Given these complexities, it clearly seems important for a future theoretical study to be conducted to determine to what degree the observed chromaticities in CQVs match, or do not match, expectations from radiative transfer. This issue has a key ability to resolve the question of whether the CQVs are caused by dust, or by gas. This question has direct bearing on the potential utility of these objects.

5.4.2. The lifetime constraint

Independent of the microphysical basis for gas absorption, the observed lifetime of the CQV phenomenon could provide another dimension to discern between the gas vs. dust clump scenarios. Based on the available statistics from the studies by L. Rebull and J. Stauffer, it seems plausible that CQV occurrence decreases in time, bottoming to zero well before the ≈ 700 Myr age of Praesepe. This is odd in the context of the prominence scenario, because pre-main-sequence M-dwarfs spin up over the first $\approx 10^8$ yr; prominences might even be expected to be more common at the age of the Pleiades than for younger stars. This broadly assumes that any star that can support prominences will, which translates in detail to a condition on the star’s mass, rotation period, and magnetic field strength. Based on the degree to which M-dwarfs remain rapid rotators over the first 700 Myr (e.g. Figure 13 of Rebull et al. 2022), it seems surprising in the gas clump (prominence) scenario that no stars older than 150 Myr have been seen to exhibit the phenomenon. In the dust clump scenario this is not a problem, because if the dust were externally sourced, it would be expected to have a finite supply.

5.5. Planets or planetesimal swarms near corotation?

Planet occurrence rate studies based on Kepler showed that around (early) M-dwarfs, there are ≈ 0.1 planets per star with sizes between $1-4 R_{\oplus}$ and orbital periods within 3 days (Dressing & Charbonneau 2015). The number increases to ≈ 0.7 planets per star, for planets with $1-4 R_{\oplus}$ and $P < 10$ days. Extrapolating to all small close-in planets, with say $0.1-4 R_{\oplus}$ and within 10 days, it is reasonable to expect on average one planet per M-dwarf. TRAPPIST-1b ($P=1.5$ days) is one example of this type of planet, in orbit around a $0.08 M_{\odot}$ star (Gillon et al. 2017).

In the context of planet formation theory, the locations of these close-in planets are set by the location of the protoplanetary disk’s magnetospheric truncation radius (see e.g. CITE for a review). In simple 1-D viscous accretion models, this truncation radius roughly coincides with the corotation radius

(CITE), though in detail factors of a few difference have been observed between the two (CITE IR studies). Within models that have migrating compact multiplanet resonant chains, the inner-most planets arrive within \approx 5-10 stellar radii within the first 100 Myr (Izidoro & Raymond 2018).

Given this context, it is tempting to try to interpret features of the CQV light curves in terms of the possible presence of close-in exoplanets, or even planetesimals. Rocky planets this young would likely have molten global magma oceans analogous to those that existed on the Earth and Moon (see Lichtenberg et al. 2022), and thus would be undergoing significant outgassing and atmospheric escape. However while a scenario in which close-in rocky planets or planetesimals serve as a possible source of dust for the clouds is *a priori* plausible, any evidence in support of such a picture currently seems ambiguous at best.

In systems like LP 12-502, the observed dip depth variations would necessarily drive one toward a picture of a disintegrating planetesimal swarm, rather than just a single planetesimal. While the number of free parameters in this type of model is somewhat dizzying, we have no right to believe that nature need be simple. The need for a swarm rather than just one launching body would be driven by the observation that we see dips appear and disappear at many *different phases*, but with roughly the same period. The observed changing dip depths in response to flares would be understood through the planetesimal outflow rates being stalled by changes in the local magnetic field or coronal plasma density. The sizes of these purported planetesimals would need to be $\lesssim 1 R_{\oplus}$, based on the non-detections of their transits, analogous to e.g. K2-22 (Sanchis-Ojeda et al. 2015) or KOI-2700 (Rappaport et al. 2014). Typical sizes of bodies in the asteroid belt for instance span hundreds of meters to a few kilometers.

The planetesimal swarm model would also predict that certain orbital phases would produce recurrent dips if observed over sufficiently long timescales, since the launching planetesimal would be massive enough to remain in orbit, and similar to say K2-22 would stochastically eject material. While the regularity of the dip phases of LP 12-502 over the existing baseline (Figure 8) might agree with this prediction, for most other CQVs (Figure 4) the data seem likely to be in tension with this expectation.

There are a few additional problems for the idea of a disintegrating planetesimal swarm. First, many of the dips show asymmetries in the wrong direction relative to the naive expectation of a trailing comet tail. Invoking non-exponentially decaying dust distributions as a function of azimuth might be one way out of this, but such an idea would need stronger theoretical footing. Dynamical stability would be a separate concern: in a model in which any new dip is “explained” by invoking a new planetesimal, one might eventually pack the corotation radius to a degree where instability over short timescales would be guaranteed.

It is certainly possible that exoplanets or exoplanetessimals could end up being connected to the CQV phenomenon, for instance as a possible source of dust through collisions at greater separations from the star. However for the time being,

none of the CQVs that we have studied in this work seem to show clear evidence for this type of origin scenario.

5.6. From dippers to debris disks

It is amusing that in identifying the two ambiguous CQV sources in Section 3.3 with outlying SEDs (TICs 193136669 and TIC 57830249), we were prompted to reconsider our light curve-based labeling, to ultimately conclude that these sources are dippers. This episode suggests that there could be overlap between CQVs and dippers. It is also worth emphasizing that our labeling of e.g. TIC 57830249 was based on a single sector of TESS data (Sector 36) when its behavior is relatively periodic and it showed dip depths of a few percent. However in other TESS sectors (e.g. Sector 10), this source looks completely different, varying in apparent flux by a factor of two, with hardly any discernible periodicity at all.

Assessing these results against the backdrop of our increasing understanding of dippers (e.g. Cody et al. 2014; Ansdell et al. 2016; Robinson et al. 2021; Capistrant et al. 2022), it is clear that the loss of an infrared excess is associated with strong changes in a star’s optical variability. It is reasonable to imagine connections between CQVs and dippers: both classes of object can show transient flux dips that are relatively narrow in duration. The dips in both are probably associated with clumps of dust or gas. However the CQV dips are typically more periodic and less deep than those of dippers, and they display far less transience over timescales of a few to tens of cycles. This is probably because CQV stars have demonstrably less dust than (most) dipper stars. At a population level, the CQV stars are also older. A common mystery between the CQVs and dippers, in our own estimation, is how exactly the *narrowness* of the dust clumps is produced. It is not unreasonable to imagine a similar mechanism operating for both types of object, tied perhaps to a shared magnetic topology, or perhaps to a preference for dust to inspiral to the star in clumped structures.

5.7. Are half-cycles important?

The interval of half a cycle period could be significant in the context of CQVs for two reasons. The first is that for material on a circular orbit viewed edge-on, it corresponds to the interval between transit and secondary eclipse. The second is that it also corresponds to the interval over which half of the star’s surface is visible. Of the CQVs in Figures 3 and 4, a number that seems greater than random might exhibit a preference for showing dips or peaks that correspond to the half-cycle interval.

One set of CQVs shows “CQV behavior” (some form of dip complex), but which only lasts for half of any given cycle. TIC 206544316 (Sector 2) is a canonical example; TIC 405910546 (Sector 38), TIC 167664935 (Sector 38), TIC 146539195 (Sector 5), TIC 118449916 (Sector 44), and TIC 312410638 (Sector 38) seem to show essentially the same tendency.

An independent set of CQVs exhibits small dips roughly half a cycle after large dips; it is tempting to label

the small dips secondary eclipses. Such sources include TIC 402980664 (Sector 25; relative to the sharpest, deepest minimum), TIC 89463560 (Sector 36), TIC 224283342 (Sector 2), and TIC 442571495 (Sector 12).

It is challenging to interpret the significance of such apparent regularities; the objects exhibit such a wide range of variability that for seemingly any “regularity” one might posit, it is easy to come up with counter-example objects which do not follow the trend. In other words, these half-cycle CQVs could simply be a product of the human tendency to pattern match; alternatively, they might yield some important physical significance.

5.8. Mass flux estimate

We can estimate the mass of a transiting cloud by first converting the transit depth to an effective cloud radius, R_{cloud} . For most CQVs in Figure 3, this typically yields $\approx 2\text{-}20 R_{\oplus}$. This size can be converted into a mass estimate by requiring the optical depth τ of the cloud to be at least unity and by positing some composition for the cloud. In other words, a minimum constraint on the number density follows by requiring the cloud to be optically thick. For cases like LP 12-502, this is reasonable because the transit duration implies $R_{\text{cloud}} \ll R_{\star}$. Carrying out the relevant calculation assuming the occulting material is dust grains $1\,\mu\text{m}$ in size, Sanderson et al. (2023) find minimum cloud masses of order $10^{12}\,\text{kg}$ (their Eq. 23), which scale linearly with both the optical depth and dust grain radius. This is comparable to a small asteroid; the asteroid belt itself has a mass of order $\approx 10^{21}\,\text{kg}$ (CITE). The previously discussed cool gas prominences would need to have masses of order $10^{14}\,\text{kg}$ (Collier Cameron et al. 1990), about $100\times$ larger than the requisite dust mass.

Our observations provide a direct measurement of how often dips appear and disappear, both due to sudden state-switches, and due to more gradual, secular evolution. For instance, LP 12-502 showed three “state-switch” events over the six months of available TESS observations, during cycles 248-264, 299-315, and 1233-1247. In each case, a dip “turned off”. It is plausible to imagine that these events correspond to either mass being ejected from corotation, or perhaps being accreted onto the star. In either case, the corresponding $\dot{M} \equiv M \cdot dN/dt$ time-averaged over six months is $\approx 3 \times 10^{-18} M_{\odot}\,\text{yr}^{-1} \approx 1 \times 10^{-12} M_{\oplus}\,\text{yr}^{-1}$. Considered cumulatively over the $\approx 10^8$ years for which the CQV phenomenon is observed, this yields a cumulative moved dust mass of $10^{-4} M_{\oplus}$, of order the Solar System’s asteroid belt. If the occulting material is gas, the masses involved would be of order 100 times larger. For cases in which we observe the *growth* of dips, such as the Sector 29 data for TIC 224283342, or Sector 5 of TIC 294328885, the dip depths typically increase by of order a few percent over ten to twenty days. This growth rate yields a mass flux one order of magnitude larger than the earlier estimate.

6. CONCLUSIONS

In this work, we searched 120-second cadence TESS data collected between July 2018 and Sep 2022 for complex quasiperiodic variables (CQVs). Our search sample included 65,760 K- and M-dwarfs within 150 pc, and was $\gtrsim 80\%$ complete within 30 pc, and $\lesssim 10\%$ complete at distances exceeding 100 pc.

In this sample of stars, we found 53 objects that showed complex quasiperiodic behavior over at least one TESS sector. Because the TESS 120-second stellar sample was rooted in a heterogeneous selection function that may have been biased in favor of young stars over field stars, we caution against interpreting our detection fraction in terms of broader population statistics. The 53 bona fide CQVs are listed in Table 1. This table also includes an additional 17 ambiguous CQVs, whose designation is less certain.

Analyzing the TESS light curves and stellar properties of these objects, we draw the following conclusions.

1. CQVs are quasiperiodic. The mean periods remain fixed over the $>1,000$ -cycle baseline of available observations; but the light curve shapes always evolve (Figure 4).
2. The same CQV can show dips with similar but clearly distinct periods. LP 12-502, for instance, showed dips with four distinct periods within $\pm 0.3\%$ of its fundamental period, sometimes simultaneously, and each lasting for up to 50 cycles (Figure 9).
3. CQVs evolve over timescales that are both secular (>100 cycles) and impulsive (<1 cycle). “State-switches” can cause dips to collapse instantaneously, and are often but not exclusively linked with observed optical flares. Dip growth however seems to happen over durations of at least ten cycles, and slow dip decay can also occur.
4. The rate of dip evolution can be used to place a model-dependent constraint on amount of material that is either being accreted or ejected during the state changes (Section 5.8). Order of magnitude estimates require at least an asteroid belt’s worth of dust ($10^{-4} M_{\oplus}$) over 10^8 years, or 100 times more material if the occulting matter is gas.
5. The CQV phenomenon persists for $\gtrsim 150$ Myr, based on the existence of multiple CQVs in AB Dor, the Pleiades, and Psc-Eri (Section 2.3). It may even extend to 200 Myr, based on the one CQV we found in the Carina Near moving group (TIC 294328887; ≈ 200 Myr). The lack of detected CQVs in the Hyades and Praesepe suggests that the lifetime of the phenomenon is likely limited to the first few hundred million years.
6. The duty cycle for CQVs seems to be $\approx 75\%$, based on the fraction of bona fide CQVs that turned on or turned off during TESS re-observations, two years after their initial observation.
7. While the majority of detected CQVs have masses of $0.1\text{-}0.5 M_{\odot}$, the upper mass limit for the CQV phenomenon might extend into the K-dwarf regime ($<0.8 M_{\odot}$).

TIC 405754448 and TIC 405910546, with masses of ≈ 0.8 and ≈ 0.6 solar masses, are the two massive outliers (Section 5.1), and we encourage additional scrutiny of these objects in future work.

8. The closest CQVs to the Sun are at distances of 15-20 pc, and the brightest CQVs have $V \approx 12$ ($J \approx 7.5$). This conclusion is an extrapolation from the CQV sample derived in this work being $\gtrsim 80\%$ complete within 20 pc. Expanding our analysis of the TESS data to the full frame images would yield a truly volume-limited selection function, and would expand the CQV census by about a factor of two within 50 pc, and by a factor of ten within 100 pc.

While many questions remain, two in particular will be important for clarifying what these objects might teach us in a broader astrophysical context: 1) Is the eclipsing material responsible for the phenomenon gas or dust? 2) What sets the characteristic clumping size for the circumstellar material?

The distinction between gas or dust is important because it will clarify whether the CQV phenomenon is intrinsic, so that the material comes from the star, or extrinsic, so that it is sourced through some generic evolutionary phase of circumstellar disks. This knowledge would in turn propagate to our understanding of whether observing the phenomenon is primarily teaching us about e.g. dust production and processing in circumstellar disks, or whether it is teaching us about the ability of cold gas to remain stable in hot stellar coronae for long durations. Observationally, acquisition of medium- or high-resolution time-series spectroscopy holds the best chance at resolving the gas vs. dust question. Given the observed evolutionary timescales, such data should be acquired simultaneously with photometric time-series observations to help clarify its interpretation.

In both the gas and dust scenarios, CQVs are preferentially viewed edge-on. This implies that after correcting for the line-of-sight inclination, at least one third of low mass stars (Günther et al. 2022) trap circumstellar material in the same way. In addition, CQVs should preferentially show edge-on transiting planets, at larger distances from the star than the corotating material. Given the interest level inherent to both of these points, important follow-up observational work also includes searching for outer transiting planets, and measuring equatorial velocities in order to test whether the stellar inclination angles are indeed preferentially edge-on.

On the theoretical front, building a physical understanding what sets the characteristic size scale of the clumping material would help clarify the nature of the magnetic and plasma environments around these young stars, and would also help build intuition for why the light curves have the bizarre shapes that are observed. The relevant puzzles in plasma physics and radiative transfer could likely be connected to our understanding of the close-in rocky planets that are expected to be present around most of these stars. The challenges intrinsic to both the observational and theoretical work seem worth the effort.

ACKNOWLEDGMENTS

LGB gratefully acknowledges support from the Heising-Simons 51 Pegasi b Fellowship. While many conversations helped encourage this work, a few thank-yous in particular (from LGB) are owed to G. Laughlin, A. Mann, and J. Speake for clarifications and ideas. This paper relies on data collected by the TESS mission, which are publicly available from the Mikulski Archive for Space Telescopes (MAST). Funding for the TESS mission is provided by NASA’s Science Mission Directorate. TIC 402980664 in particular was observed at 120-second cadence thanks to the TESS Guest Investigator programs G022252 (PI: J. Schlieder; Sectors 18, 19, 25, 26) and G04168 (PI: R. Jayaraman; Sector 53).

DRAFT AUTHOR CONTRIBUTION STATEMENTS

- PLEASE REVISE IF APPROPRIATE) LGB and RJ conceived the project and executed the dip-based and Fourier-based searches, respectively. LGB drafted the initial manuscript, and performed the cluster membership, SED, and variability analyses. SR and RJ vetted the results from the Fourier search. LAH advised on project scope and experiment design. GÁB acquired and maintained the servers used to run the dip-finding pipeline. GRR is an architect of the TESS mission. All authors assisted in manuscript revision.

Software: astrobase (Bhatti et al. 2021), lightkurve (Lightkurve Collaboration et al. 2018), scipy (Virtanen et al. 2020), TESS-point (Burke et al. 2020),

Facilities: *Astrometry:* Gaia (Gaia Collaboration et al. 2018, 2022). *Imaging:* Second Generation Digitized Sky Survey. *Spectroscopy:* Keck:I (HIRES; Vogt et al. 1994). *Photometry:* TESS (Ricker et al. 2015), Broadband photometry: 2MASS (Skrutskie et al. 2006), APASS (Henden et al. 2016), Gaia (Gaia Collaboration et al. 2018, 2022), SDSS (York et al. 2000), WISE (Wright et al. 2010).

REFERENCES

- Allard, F., Homeier, D., & Freytag, B. 2012, Philosophical Transactions of the Royal Society A: Mathematical, Physical and Engineering Sciences, 370, 2765
- Ansdell, M., Gaidos, E., Rappaport, S. A., et al. 2016, ApJ, 816, 69
- Apai, D., Nardiello, D., & Bedin, L. R. 2021, ApJ, 906, 64

- Asplund, M., Grevesse, N., Sauval, A. J., & Scott, P. 2009, ARA&A, 47, 481
- Bailer-Jones, C. A. L., Rybizki, J., Fouesneau, M., Demleitner, M., & Andrae, R. 2021, AJ, 161, 147
- Barber, R. J., Tennyson, J., Harris, G. J., & Tolchenov, R. N. 2006, MNRAS, 368, 1087

- Basri, G. 2021, An Introduction to Stellar Magnetic Activity
- Bell, C. P. M., Mamajek, E. E., & Naylor, T. 2015, *MNRAS*, **454**, 593
- Berry, I. D., Owocki, S. P., Shultz, M. E., & ud-Doula, A. 2022, *MNRAS*, **511**, 4815
- Bhatti, W., Bouma, L., Joshua, et al. 2021, waqasbhatti/astrobase: astrobase v0.5.3, Zenodo
- Bodman, E. H. L., Quillen, A. C., Ansdell, M., et al. 2017, *MNRAS*, **470**, 202
- Bouma, L. G., Winn, J. N., Ricker, G. R., et al. 2020, *AJ*, **160**, 86
- Bouma, L. G., Curtis, J. L., Masuda, K., et al. 2022, *AJ*, **163**, 121
- Boyle, A. W., & Bouma, L. G. 2023, *AJ*, **166**, 14
- Bressan, A., Marigo, P., Girardi, L., et al. 2012, *MNRAS*, **427**, 127
- Brogi, M., Keller, C. U., de Juan Ovelar, M., et al. 2012, *A&A*, **545**, L5
- Burke, C. J., Levine, A., Fausnaugh, M., et al. 2020, TESS-Point: High precision TESS pointing tool, Astrophysics Source Code Library, record ascl:2003.001
- Capistrant, B. K., Soares-Furtado, M., Vanderburg, A., et al. 2022, *ApJS*, **263**, 14
- Cardelli, J. A., Clayton, G. C., & Mathis, J. S. 1989, *ApJ*, **345**, 245
- Chen, Y., Girardi, L., Bressan, A., et al. 2014, *MNRAS*, **444**, 2525
- Cody, A. M., Stauffer, J., Baglin, A., et al. 2014, *AJ*, **147**, 82
- Collier Cameron, A. 1999, in Astronomical Society of the Pacific Conference Series, Vol. 158, Solar and Stellar Activity: Similarities and Differences, ed. C. J. Butler & J. G. Doyle, 146
- Collier Cameron, A., Duncan, D. K., Ehrenfreund, P., et al. 1990, *MNRAS*, **247**, 415
- Collier Cameron, A., & Robinson, R. D. 1989, *MNRAS*, **238**, 657
- Curtis, J. L., Agüeros, M. A., Mamajek, E. E., Wright, J. T., & Cummings, J. D. 2019, *AJ*, **158**, 77
- Dahm, S. E. 2015, *ApJ*, **813**, 108
- David, T. J., & Hillenbrand, L. A. 2015, *ApJ*, **804**, 146
- Dressing, C. D., & Charbonneau, D. 2015, *ApJ*, **807**, 45
- Dunstone, N. J., Barnes, J. R., Collier Cameron, A., & Jardine, M. 2006, *MNRAS*, **365**, 530
- Fausnaugh, M., Morgan, E., Vanderspek, R., et al. 2021, *PASP*, **133**, 095002
- Feiden, G. A. 2016, *A&A*, **593**, A99
- Ferreira, J. M. 2000, *MNRAS*, **316**, 647
- Gagné, J., Mamajek, E. E., Malo, L., et al. 2018, *ApJ*, **856**, 23
- Gaia Collaboration, Brown, A. G. A., Vallenari, A., et al. 2018, *A&A*, **616**, A1
- Gaia Collaboration, Vallenari, A., Brown, A. G. A., et al. 2022, *arXiv e-prints*, arXiv:2208.00211
- Gillon, M., Triaud, A. H. M. J., Demory, B.-O., et al. 2017, *Nature*, **542**, 456
- Gray, D. F. 1992, The observation and analysis of stellar photospheres., Vol. 20
- Gully-Santiago, M. A., Herczeg, G. J., Czekala, I., et al. 2017, *ApJ*, **836**, 200
- Günther, M. N., Berardo, D. A., Ducrot, E., et al. 2022, *AJ*, **163**, 144
- Henden, A. A., Templeton, M., Terrell, D., et al. 2016, VizieR Online Data Catalog, II/336
- Hesser, J. E., Ugarte, P. P., & Moreno, H. 1977, *ApJL*, **216**, L31
- Hippke, M., David, T. J., Mulders, G. D., & Heller, R. 2019, *AJ*, **158**, 143
- Izidoro, A., & Raymond, S. N. 2018, in Handbook of Exoplanets, ed. H. J. Deeg & J. A. Belmonte, 142
- Jardine, M., & Collier Cameron, A. 2019, *MNRAS*, **482**, 2853
- Jeffries, R. D. 1993, *MNRAS*, **262**, 369
- Jenkins, J. M., Twicken, J. D., McCauliff, S., et al. 2016, in Society of Photo-Optical Instrumentation Engineers (SPIE) Conference Series, Vol. 9913, Software and Cyberinfrastructure for Astronomy IV, ed. G. Chiozzi & J. C. Guzman, 99133E
- Justesen, A. B., & Albrecht, S. 2021, *ApJ*, **912**, 123
- Kenyon, S. J., & Hartmann, L. 1995, *ApJS*, **101**, 117
- Kerr, R. M. P., Rizzuto, A. C., Kraus, A. L., & Offner, S. S. R. 2021, *ApJ*, **917**, 23
- Koen, C. 2021, *MNRAS*, **500**, 1366
- . 2023, *MNRAS*, **518**, 2921
- Leitzinger, M., Odert, P., Zaqrashvili, T. V., et al. 2016, *MNRAS*, **463**, 965
- Lichtenberg, T., Schaefer, L. K., Nakajima, M., & Fischer, R. A. 2022, *arXiv e-prints*, arXiv:2203.10023
- Lightkurve Collaboration, Cardoso, J. V. d. M., Hedges, C., et al. 2018, Lightkurve: Kepler and TESS time series analysis in Python, Astrophysics Source Code Library, record ascl:1812.013
- MacLeod, M., & Oklopčić, A. 2022, *ApJ*, **926**, 226
- McCann, J., Murray-Clay, R. A., Kratter, K., & Krumholz, M. R. 2019, *ApJ*, **873**, 89
- Meingast, S., Alves, J., & Rottensteiner, A. 2021, *A&A*, **645**, A84
- Murphy, S. J., Lawson, W. A., & Bessell, M. S. 2013, *MNRAS*, **435**, 1325
- Palumbo, E. K., Montet, B. T., Feinstein, A. D., et al. 2022, *ApJ*, **925**, 75
- Pecaut, M. J., & Mamajek, E. E. 2013, *ApJS*, **208**, 9
- . 2016, *MNRAS*, **461**, 794
- Popinchalk, M., Faherty, J. K., Curtis, J. L., et al. 2023, *ApJ*, **945**, 114
- Rajpurohit, A. S., Reylé, C., Allard, F., et al. 2013, *A&A*, **556**, A15
- Rappaport, S., Barclay, T., DeVore, J., et al. 2014, *ApJ*, **784**, 40
- Rappaport, S., Levine, A., Chiang, E., et al. 2012, *ApJ*, **752**, 1
- Ratzenböck, S., Meingast, S., Alves, J., Möller, T., & Bomze, I. 2020, *A&A*, **639**, A64
- Rebull, L. M., Stauffer, J. R., Cody, A. M., et al. 2018, *AJ*, **155**, 196

- Rebull, L. M., Stauffer, J. R., Hillenbrand, L. A., et al. 2022, *AJ*, **164**, 80
- Rebull, L. M., Stauffer, J. R., Bouvier, J., et al. 2016, *AJ*, **152**, 114
- Ricker, G. R., Winn, J. N., Vanderspek, R., et al. 2015, *Journal of Astronomical Telescopes, Instruments, and Systems*, **1**, 014003
- Robinson, C. E., Espaillat, C. C., & Owen, J. E. 2021, *ApJ*, **908**, 16
- Rodriguez, D. R., van der Plas, G., Kastner, J. H., et al. 2015, *A&A*, **582**, L5
- Sanchis-Ojeda, R., Rappaport, S., Pallè, E., et al. 2015, *ApJ*, **812**, 112
- Sanderson, H., Jardine, M., Collier Cameron, A., Morin, J., & Donati, J. F. 2023, *MNRAS*, **518**, 4734
- Skrutskie, M. F., Cutri, R. M., Stiening, R., et al. 2006, *AJ*, **131**, 1163
- Somers, G., Cao, L., & Pinsonneault, M. H. 2020, *ApJ*, **891**, 29
- Speagle, J. S. 2020, *MNRAS*, **493**, 3132
- Stassun, K. G., Kratter, K. M., Scholz, A., & Dupuy, T. J. 2012, *ApJ*, **756**, 47
- Stassun, K. G., Oelkers, R. J., Pepper, J., et al. 2018, *AJ*, **156**, 102
- Stauffer, J., Collier Cameron, A., Jardine, M., et al. 2017, *AJ*, **153**, 152
- Stauffer, J., Rebull, L., David, T. J., et al. 2018, *AJ*, **155**, 63
- Stellingwerf, R. F. 1978, *ApJ*, **224**, 953
- Townsend, R. H. D., & Owocki, S. P. 2005, *MNRAS*, **357**, 251
- Townsend, R. H. D., Owocki, S. P., & Groote, D. 2005, *ApJL*, **630**, L81
- Vanderburg, A., Johnson, J. A., Rappaport, S., et al. 2015, *Nature*, **526**, 546
- Vial, J.-C., & Engvold, O. 2015, *Astrophysics and Space Science Library*, Vol. 415, Solar Prominences
- Vines, J. I., & Jenkins, J. S. 2022, *MNRAS*, **513**, 2719
- Virtanen, P., Gommers, R., Oliphant, T. E., et al. 2020, *Nature Methods*, **17**, 261
- Vogt, S. S., Allen, S. L., Bigelow, B. C., et al. 1994, in *Society of Photo-Optical Instrumentation Engineers (SPIE) Conference Series*, Vol. 2198, *Instrumentation in Astronomy VIII*, ed. D. L. Crawford & E. R. Craine, 362
- Vos, J. M., Faherty, J. K., Gagné, J., et al. 2022, *ApJ*, **924**, 68
- Waugh, R. F. P., & Jardine, M. M. 2022, *MNRAS*, **514**, 5465
- Winn, J. N. 2010, in *Exoplanets*, ed. S. Seager, 55
- Wishart, A. W. 1979, *MNRAS*, **187**, 59P
- Wright, E. L., Eisenhardt, P. R. M., Mainzer, A. K., et al. 2010, *AJ*, **140**, 1868
- York, D. G., Adelman, J., Anderson, John E., J., et al. 2000, *AJ*, **120**, 1579
- Zhan, Z., Günther, M. N., Rappaport, S., et al. 2019, *ApJ*, **876**, 127
- Zieba, S., Zwintz, K., Kenworthy, M. A., & Kennedy, G. M. 2019, *A&A*, **625**, L13
- Zuckerman, B. 2019, *ApJ*, **870**, 27
- Zuckerman, B., Bessell, M. S., Song, I., & Kim, S. 2006, *ApJL*, **649**, L115

Table 1. Complex quasiperiodic variables identified in the TESS 2-minute data. **For internal review, full versions are available here** <https://www.dropbox.com/scl/fo/twn4s9ckbevf75jqhtoy1/h?rlkey=t5cn8cx2uoc2ptdm9e570kp1b&dl=0>

TIC	<i>T</i>	<i>d</i>	$G_{\text{BP}} - G_{\text{RP}}$	RUWE	<i>P</i>	Assoc	Age	T_{eff}	R_{\star}	M_{\star}	R_{cr}	Quality	N_{sector}
–	mag	pc	mag	–	hr	–	Myr	K	R_{\odot}	M_{\odot}	R_{\star}	–	–
368129164	9.29	18.3	2.9	6.95	6.44	ABDMG	149	3140	0.71	0.4	1.81	1	3
405754448	9.63	96.5	1.75	4.66	12.92	LCC	15	4273	1.5	0.82	1.74	1	5
167664935	10.31	63.0	2.52	1.62	14.05	UCL	16	3325	1.42	0.38	1.5	1	3
311092148	11.03	26.9	3.04	1.31	7.86	COL	42	3035	0.5	0.27	2.6	1	1
402980664	11.11	21.3	3.05	1.26	18.56	COL	42	3080	0.37	0.22	5.76	1	10
50745567	11.28	38.5	3.23	1.84	6.34	BPMG	24	3014	0.67	0.28	1.68	1	2
425933644	11.4	44.3	2.83	2.29	11.67	THA	45	3151	0.63	0.4	3.06	1	6
142173958	11.61	72.6	3.1	1.43	11.76	TWA	10	3028	1.15	0.26	1.45	1	3
146539195	11.62	48.6	3.38	1.59	6.73	BPMG	24	2898	0.8	0.24	1.38	1	2
206544316	11.63	43.1	2.89	1.27	7.73	THA	45	3114	0.57	0.35	2.44	1	6
335598085	11.9	105.9	2.86	1.64	15.85	LCC	15	3119	1.34	0.28	1.56	1	3
405910546	12.11	112.2	2.36	1.09	37.99	LCC	15	3455	0.92	0.6	5.26	1	4
272248916	12.15	80.3	2.84	3.18	8.9	UCL	16	3193	0.81	0.4	1.97	1	3
178155030	12.17	46.8	2.91	1.23	11.67	THA	45	3097	0.49	0.3	3.53	1	4
224283342	12.29	38.1	3.04	1.24	21.3	COL	42	3050	0.39	0.22	6.08	1	3
89026133	12.31	139.2	2.82	2.4	11.2	UCL	16	3188	1.33	0.31	1.29	1	3
234295610	12.51	48.2	3.05	1.13	18.29	THA	45	3074	0.44	0.27	5.09	1	3
118449916	12.54	69.2	3.1	8.17	12.31	TAU	2	3025	1.04	0.28	1.7	1	4
67897871	12.55	145.5	3.02	1.67	6.23	USCO	10	3082	1.5	0.18	0.65	1	2
353730181	12.65	107.3	2.75	1.17	13.51	TAU	2	3253	0.8	0.41	2.65	1	4
201898222	12.68	42.2	3.22	1.14	10.7	THA	45	2996	0.39	0.2	3.69	1	5
264767454	12.73	112.6	2.93	16.58	10.01	COL	42	3150	1.0	0.42	1.76	1	13
442571495	12.75	78.5	3.03	1.38	9.59	UCL	16	3099	0.65	0.3	2.35	1	3
2234692	12.8	53.6	3.0	1.08	6.52	COL	42	3098	0.44	0.26	2.56	1	7
94088626	12.88	57.8	3.06	1.1	6.6	ARG	45	3090	0.46	0.27	2.53	1	2
264599508	12.88	80.0	3.0	1.53	7.9	COL	42	3098	0.62	0.4	2.4	1	7
363963079	12.92	81.8	3.1	5.57	7.82	ARG	45	3040	0.67	0.4	2.21	1	7
193831684	13.03	51.5	3.2	1.06	31.02	BPMG	24	2971	0.42	0.2	6.87	1	3
177309964	13.1	91.1	2.93	1.31	10.88	CAR	45	3125	0.62	0.4	2.95	1	34
425937691	13.18	43.8	3.79	1.69	4.82	THA	45	2782	0.41	0.16	1.91	1	5
141146667	13.28	57.5	3.29	1.18	3.93	FIELD	NaN	2968	0.42	NaN	NaN	1	6
332517282	13.29	39.1	3.29	0.93	9.67	ABDMG	149	2975	0.28	0.2	4.87	1	3
144486786	13.3	70.4	3.07	7.62	6.82	COL	42	3074	0.51	0.3	2.38	1	4
38820496	13.3	44.1	3.38	1.21	15.73	THA	45	2903	0.34	0.16	5.13	1	5
289840926	13.31	40.2	3.76	1.0	4.8	BPMG	24	2807	0.36	0.14	2.05	1	3
404144841	13.33	76.0	3.2	1.03	10.74	TWA	10	3008	0.52	0.22	2.86	1	4
89463560	13.45	126.9	2.97	1.31	9.43	ARG	45	3055	0.75	0.37	2.15	1	10
300651846	13.49	109.6	2.87	1.25	8.26	CAR	45	3136	0.62	0.4	2.44	1	31
267953787	13.49	130.6	3.58	1.09	17.46	TAU	2	2826	1.06	0.12	1.59	1	4
58084670	13.58	140.6	2.81	1.04	11.16	FIELD	NaN	3138	0.77	NaN	NaN	1	6
68812630	13.6	132.7	3.24	1.24	9.04	TAU	2	2996	0.76	0.27	1.86	1	3
141306513	13.65	50.0	3.42	1.23	13.36	THA	45	2964	0.32	0.16	4.85	1	2
5714469	13.73	78.4	3.66	1.07	10.35	UCL	16	2828	0.54	0.18	2.53	1	3

Table 1 *continued*

Table 1 (*continued*)

201789285	14.03	45.2	3.85	1.18	3.64	THA	45	2757	0.3	0.12	2.02	1	5
294328887	14.23	97.8	3.23	1.11	8.51	CARN	200	2994	0.45	0.35	3.33	1	35
302160226	14.24	147.6	3.07	1.16	7.88	APER	86	3065	0.62	0.4	2.4	1	2
312410638	14.3	138.8	3.14	1.11	28.06	UCL	16	3030	0.58	0.25	5.11	1	3
251496897	14.36	115.0	3.0	1.11	8.38	ARG	45	3100	0.44	0.27	3.04	1	2
38539720	14.52	132.1	3.38	1.27	9.16	PERI	120	2924	0.57	0.25	2.43	1	1
359892714	14.53	94.0	3.99	1.18	11.33	EPSC	3	2675	0.55	0.13	2.36	1	6
118769116	14.58	120.3	3.6	1.11	8.56	TAU	2	2852	0.56	0.2	2.18	1	4
440725886	14.69	131.6	2.94	1.23	3.92	PLE	112	3109	0.45	0.35	1.99	1	5
397791443	15.01	149.5	3.07	1.05	6.95	LCC	15	3031	0.48	0.22	2.32	1	6
160329609	9.65	8.7	3.41	1.28	24.31	ARG	45	2912	0.35	0.16	6.6	0	3
59836633	11.38	62.1	2.72	1.18	14.96	BPMG	24	3282	0.82	0.48	2.91	0	3
435903839	11.95	92.4	2.48	11.63	10.82	ABDMG	149	3458	0.76	0.54	2.66	0	6
57830249	11.96	48.7	3.21	1.27	43.82	TWA	10	2948	0.7	0.25	5.63	0	3
148646689	12.14	142.4	2.44	2.24	10.63	UCL	16	3466	1.25	0.55	1.61	0	3
280945693	12.27	98.3	2.97	1.1	15.27	LCC	15	3103	1.09	0.31	1.94	0	5
149838027	12.28	44.2	3.07	1.33	12.89	THA	45	3051	0.46	0.26	3.83	0	3
165184400	12.37	43.1	3.03	1.14	15.91	THA	45	3076	0.42	0.25	4.74	0	4
245834739	12.55	110.5	2.85	1.25	10.47	TAU	2	3112	1.02	0.36	1.68	0	6
125843782	13.01	128.5	2.87	0.99	44.17	TAU	2	3135	0.9	0.35	4.97	0	4
193136669	13.06	61.3	3.51	1.08	37.64	TWA	10	2855	0.58	0.19	5.62	0	4
244161191	13.17	44.4	3.54	1.33	7.17	COL	42	2860	0.38	0.18	2.8	0	3
231058925	13.17	51.1	3.26	1.15	8.87	THA	45	2978	0.38	0.2	3.33	0	5
245874053	13.26	142.2	3.2	1.18	25.98	TAU	2	3017	1.16	0.26	2.45	0	4
301676454	13.4	71.1	3.07	1.35	9.18	ARG	45	3009	0.47	0.25	2.96	0	1
67745212	13.63	27.7	3.82	1.09	5.12	COL	42	2781	0.21	0.09	3.17	0	2
259586708	13.82	96.3	2.93	1.22	22.52	COL	42	3133	0.46	0.29	5.84	0	7

NOTE—This table includes 53 CQVs (Quality flag true), and 17 ambiguous CQVs (Quality flag false). The machine-readable version, available online, includes additional columns for the Gaia DR2 source identifiers and parameter uncertainties. The age uncertainties are typically $\approx \pm 10\%$, but can be asymmetric. The median temperature, radius, and mass uncertainties are $\pm XXX$ K, $\pm XX\%$, and $\pm YY\%$ respectively. N_{sector} denotes the number of TESS sectors for which data are expected to be acquired between July 2018 and Oct 2024. Association names and provenance follow conventions adopted by Gagné et al. (2018): ABDMG: AB Doradus moving group (Bell et al. 2015). ARG: Argus (Zuckerman 2019). APER: α Persei open cluster (Boyle & Bouma 2023). BPMG: β Pic moving group (Bell et al. 2015). CARN: Carina Near moving group (Zuckerman et al. 2006). COL: Columba (Bell et al. 2015). EPSC: ϵ Chamaeleontis (Murphy et al. 2013). LCC: Lower Centaurus Crux (Pecaut & Mamajek 2016). PERI: Pisces-Eridani (Curtis et al. 2019). PLE: Pleiades (Dahm 2015). TAU: Taurus (Kenyon & Hartmann 1995). THA: Tucana-Horologium association (Bell et al. 2015). TWA: TW Hydriæ association (Bell et al. 2015). UCL: Upper Centaurus Lupus (Pecaut & Mamajek 2016). USCO: Upper Scorpius (Pecaut & Mamajek 2016).

APPENDIX

A. LP 12-502

The light curve—Figure 8 shows another alternative view of Figure 6, but arranged to enable easy visual appreciation of transit timing changes, rather than transit depth changes. A best-fitting two-harmonic sinusoid has been independently fitted and subtracted from the Sector 18-19 data, 25-26 data, and 53, 58, and 59 data.

Finally, Figure 9 shows “river plots” of the same data, split into similar intervals: the Sector 18-19 data, 25-26 data, 53 data, and 58-59 data. State changes are evident in these plots whenever there is a sudden change in color. **todo: fix missing data to be different from the flare color**

B. MORE RIVER PLOTS

Figures 10 and 11 show 120-second cadence data for TIC 300651846, a CQV in the TESS continuous viewing zone. With the exception of a few sectors, TESS data will exist for this source over Sectors 1-12, 27-39, and 61-69. The majority are in the full frame images, and are the subject of future work.

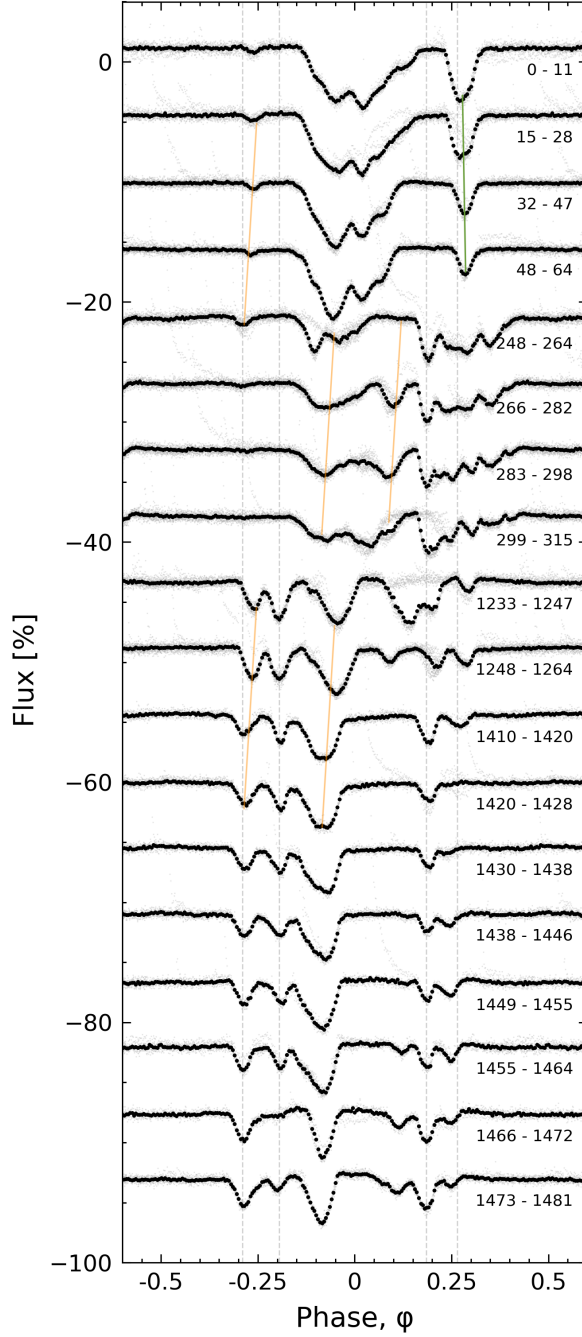


Figure 8. Alternative view of the evolution of LP 12-502 (Figure 6), arranged to emphasize changes in transit times. There are 200 binned black points per cycle; a two-harmonic sinusoid has been subtracted over specific chunks in time (see text). Vertical gray lines are underplotted to help guide the eye to instances in which preferred dip phases synchronize over long baselines. The orange and green lines guide the eye to where dips appear to change the positions of their local minima.

C. NO SIGNIFICANT POWER AT 20 SECOND CADENCE

TESS was the first instrument to show that CQV light curves contain power at timescales of a few minutes (Bouma et al. 2020; Günther et al. 2022). This advance was primarily enabled by the fifteen-fold faster cadence in the TESS 2-minute data, relative to K2.

A logical follow-up question to ask is whether the periodic components of the CQV light curves contain power at timescales below one minute. Between 2020 and 2021, we observed 10 CQVs at 20-second cadence with TESS in order to explore this ques-

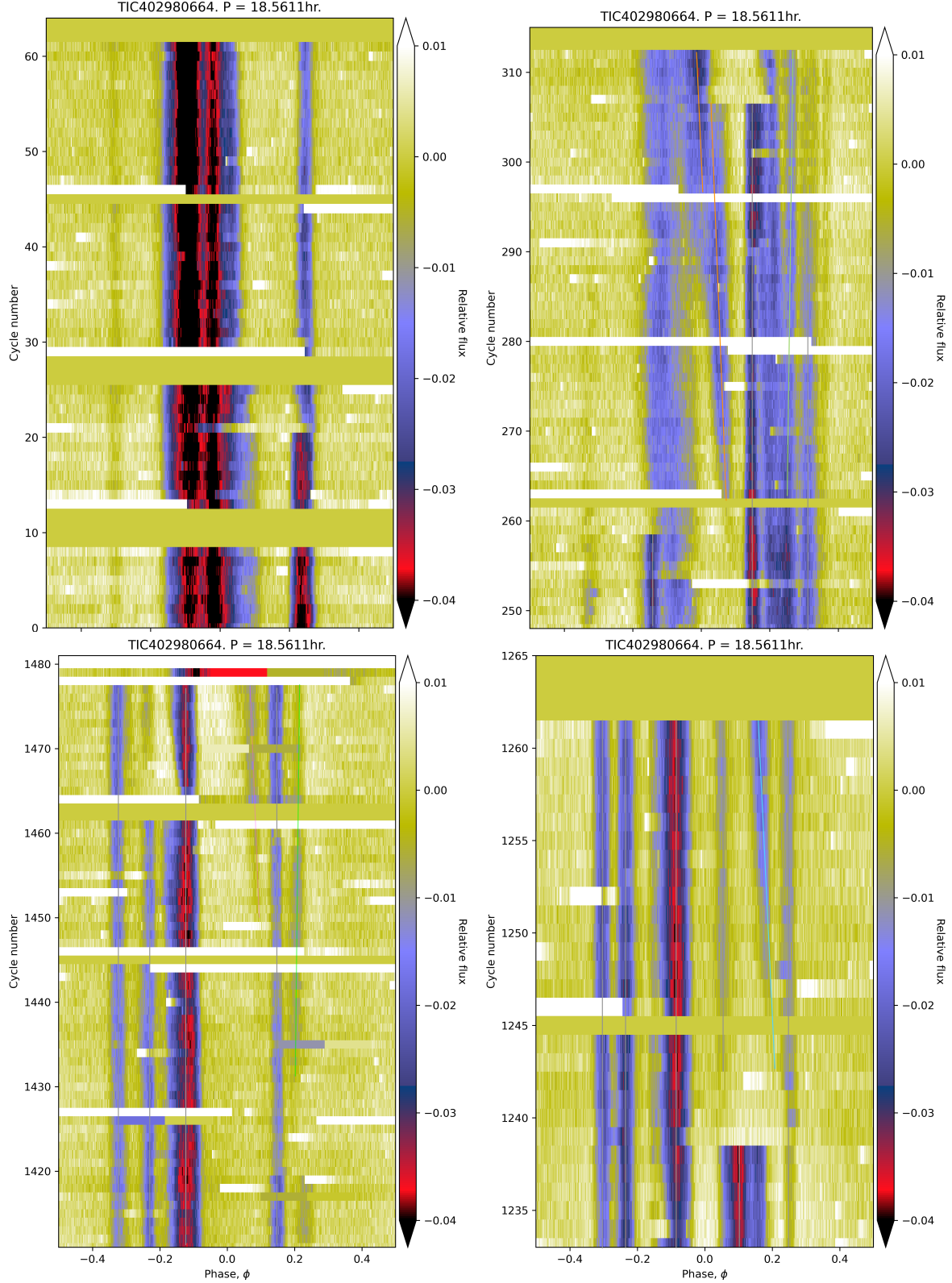


Figure 9. River plots of LP 12-502, showing (clockwise from top-left) Sectors 18-19, 25-26, 53, and 58-59. A two-harmonic sinusoid has been subtracted over specific chunks in time (see text). For Sectors 25-26 (cycles 248-315), three periods are overplotted: $P=18.5145\text{hr}$ (gray vertical line); 18.5404hr (orange); 18.5683hr (green). For Sector 53, gray is identical, while cyan is 18.5145hr . For Sectors 58-59, the magenta line is 18.5473hr , and the green line is 18.5672hr .

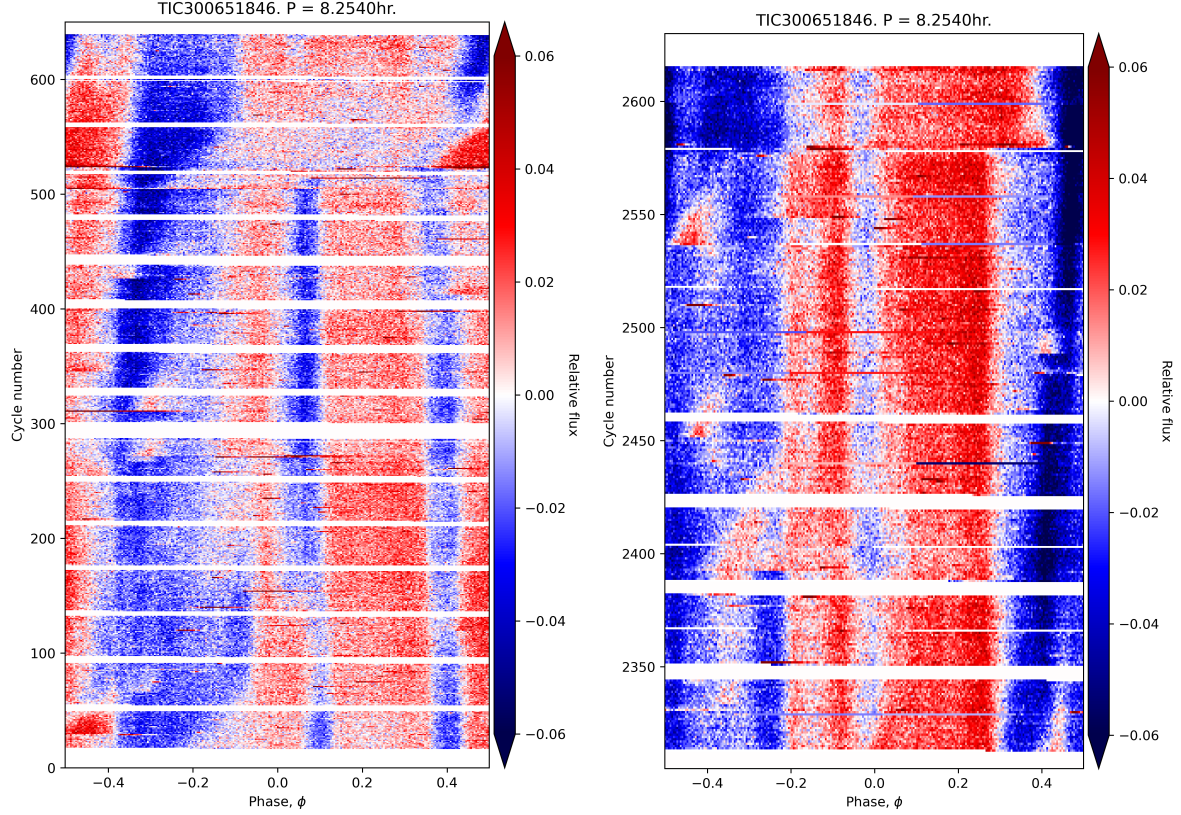


Figure 10. River plots of TIC 300651846. The envelope has not been subtracted. 7 sectors of continuous 2-minute observations S32-S39. (Thanks to DDT029) Then a few in S60+ on the right. Compare to Figure 3.

tion (TESS DDT029). The stars were TICs 142173958, 146539195, 24518895, 276453848, 264599508, 363963079, 144486786, 408188366, 300651846, 262400835. The general conclusion derived from comparing the 20-second to 120-second data for these stars (available on MAST) was that CQVs do not contain appreciable power at this timescale.

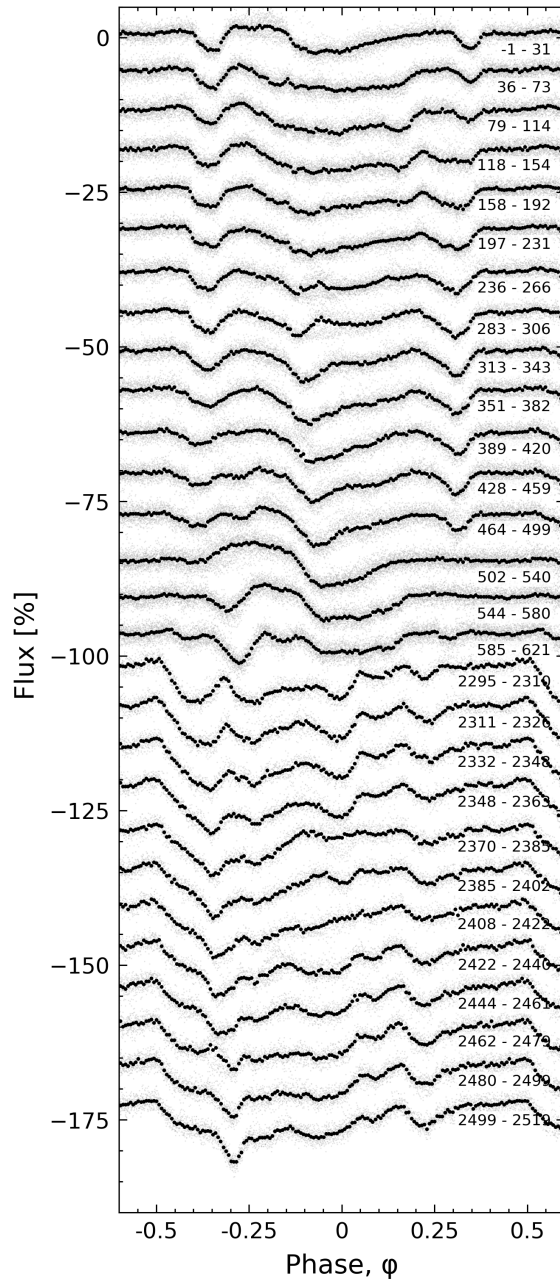


Figure 11. Orbit-phased plots of TIC 300651846. The envelope has not been subtracted.